RICE UNIVERSITY

Statistical moments of the multiplicity distributions of identified particles in Au+Au collisions

by

Daniel McDonald

A Thesis Submitted
in Partial Fulfillment of the
Requirements for the Degree

Doctor of Philosophy

Approved, Thesis Committee:

_____

W.J. Llope, Chair
Senior Faculty Fellow

_____

Marjorie D. Corcoran
Professor of Physics and Astronomy

_____

Stephen Semmes
Noah Harding Professor of Mathematics

Houston, Texas

May, 2013

ABSTRACT

Statistical moments of the multiplicity distributions of identified particles in
Au+Au collisions

by

Daniel McDonald

In part to search for a possible critical point (CP) in the phase diagram of hot
nuclear matter, a beam energy scan was performed at the Relativistic Heavy-Ion Col-
lider at Brookhaven National Laboratory. The Solenoidal Tracker at RHIC (STAR)
collected Au+Au data sets at beam energies, $\sqrt{s_{NN}}$, of 7.7, 11.5, 19.6, 27, 39, 62.4, and
200 GeV. Such a scan produces hot nuclear matter at different locations in the phase
diagram. Lattice and phenomenological calculations suggest that the presence of a
CP might result in divergences of the thermodynamic susceptibilities and correlation
lengths. The statistical moments of the identified-particle multiplicity distributions
directly depend on both the thermodynamic susceptibilities and correlation lengths,
possibly making the shapes of these multiplicity distributions sensitive tools for the
search for the critical point. The statistical moments of the multiplicity distributions
of a number of different groups of identified particle species were analyzed. Care was
taken to remove a number of experimental artifacts that can modify the shapes of the
multiplicity distributions. The observables studied include the lowest four statistical
moments (mean, variance, skewness, kurtosis) and some products of these moments.
These observables were compared to the predictions from several approaches lacking
critical behavior, such as the Hadron Resonance Gas model, mixed events, (negative)

binomial, and Poisson statistics. In addition, the data were analyzed after gating on the event-by-event antiproton-to-proton ratio, which is expected to more tightly constrain the event trajectories on the phase diagram.

Acknowledgement

Of course, I am most grateful to my wife for her patience and *love*. I would not be here without her, and she is my everything. I am still in disbelief that she married me; I am the luckiest man alive.

It has not been the easiest journey, but rarely are worthwhile journeys easy. I want people to know that anything is possible. My journey was a difficult one—growing up in a single-parent household below the poverty line, moving to the United States and adjusting to a different culture, getting in two tragic accidents that resulted in years of physical therapy, and working throughout college to pay my way. And yet here I am.

Thanks go out to those that helped me along the way. To all my friends, who are too numerous to list, thank you very much. A special thank you goes to my best friend, Danny Blanco. You are the best friend a person could ever want. Thanks for keeping my morale up during the low points and celebrating during the high points. Also, a special thank you goes to my little sister Kristina. Go us! Also, thanks to my dad. I am so glad that we grew into the close friends we are today.

Last, but certainly not least, a heartfelt thanks to my physics colleagues and friends, who are also too numerous to list. Thank you to Frank for your many insightful conversations. Thank you to Paul Stevenson, Paul Padley, and Jay Roberts for your patience during my recovery process from my bike accident and lung collapse. And finally, thank you to Bill, my advisor. I am thankful for your guidance and I am happy that we made it to the finish line.

Daniel McDonald

Contents

Illustrations

Tables

to DEB, SEB, and MRM

Chapter 1

Introduction

When nuclei are collided at high beam energies (e.g., $\sqrt{s_{NN}}^*$=200 GeV), a state of nuclear matter that is very dense and hot ($\sim$2 trillion degrees) is created. This excited system of nuclear matter is hundreds of thousands of times hotter than the sun. These violent heavy-ion collisions provide insight into the universe in the first microseconds after the Big Bang. The very dense and hot system formed in high-energy heavy-ion collisions is not envisioned as a system of nucleons but as a system of free quarks and gluons.

The first laboratory collider capable of investigating such matter is the Relativistic Heavy-Ion Collider (RHIC), located at Brookhaven National Laboratory (BNL) on Long Island, New York. RHIC is comprised of two concentric rings that are each 2.4 miles (3.8 km) in circumference. RHIC is capable of colliding a variety of particle species (Au+Au, Cu+Cu, U+U, Au+Cu, d+Au, p+p) over a wide range of beam energies (7.7-500 GeV). The first collisions at RHIC were recorded in 2000, and the collider has successfully run in every year since.

The systems formed in head-on, or "central," collisions at the highest beam energies at RHIC are so dense that they are opaque to jets, which are collimated sprays of very high energy particles resulting from parton (quark or gluon) scattering [1]. This was the first observation of matter dense enough to quench jets. In addition,

---

$^*\sqrt{s_{NN}}$ is the square root of the Mandelstam variable, s, and is the total energy in the two nucleon center of momentum system

the elliptic flow, which is a parameter characterizing the quadrupole anisotropy of the particle distributions, is different for mesons and baryons but collapses to a single universal curve when the elliptic flow is plotted versus the transverse mass and both axes are scaled by the number of constituent quarks in the meson (2) or baryon (3) [2]. This suggests that the relevant degrees of freedom are quarks, not mesons or baryons. The magnitude of the elliptic flow is also near the hydrodynamic limit, indicating that the state of matter created at RHIC is more liquid-like than gas-like. In fact, this nuclear matter is considered the most "perfect" liquid ever observed [3]. Thus, the nuclear matter created in the highest energy head-on collisions at RHIC cannot be described by hadronic degrees of freedom, and is instead better considered a strongly interacting Quark Gluon Plasma (QGP)–a very dense, fluid-like phase of matter where quarks and gluons are deconfined.

1.1 Particle multiplicities

One of the most fundamental quantities that can be experimentally measured in heavy-ion collision events is the number particles of different species that were produced. These particle multiplicities are sensitive to a number of different quantities that provide insight into the properties of nuclear matter. Three such quantities are described in the following subsections.

1.1.1 Particle multiplicities and centrality

When looking along the beam direction, the transverse distance between the centers of two colliding nuclei is known as the impact parameter. When the impact parameter is zero, the two nuclei collide "head on." This is called a "central" collision. The largest impact parameter resulting in nuclear overlap for two colliding gold nuclei is ∼14 fermi

(1 fm $= 10^{-15}$ m), or twice the 7 fm radius of a single gold nucleus. The more head-on the collisions between the two nuclei, the more nucleons participate. These nucleons are called "participants." Each nucleon-nucleon collision produces secondary particles, which can interact with other participants and other produced particles. All of the particles finally stream towards detectors, where they are measured. As the number of nucleon-nucleon collisions increases, the measured multiplicity increases. Therefore, the measured multiplicity of particles is directly related to the impact parameter. This allows one to infer the centrality of each collision from the multiplicities measured in the detectors.

Shown in Fig. 1.1 is a schematic plot of the distribution of the number of measured particles in an event over many events. The most probable events are peripheral collisions, and as the collisions become more central they become relatively more infrequent. Central collisions are on the right side of the figure and peripheral collisions are on the left side. Shown on the top axis is the average impact parameter, $\langle b \rangle$, and the average number of participating nucleons, $\langle N_{\mathrm{part}} \rangle$. These quantities are inferred from a Glauber model [4] that can reproduce this probability distribution based on the nucleon-nucleon cross section and a few free parameters. This allows one to set a cut on the observed multiplicity of charged particles that corresponds to specific ranges of the impact parameter. For example, a gate on the top 0-5% centrality corresponds, on average, to impact parameters less than 3.13 fm.

1.1.2 Event-averaged identified-particle multiplicities and the statistical hadronization model

The mean multiplicities of identified charged particles such as $\pi^{\pm}$, $K^{\pm}$, p, and $\bar{\mathrm{p}}$ can be measured experimentally. Ratios of these multiplicities can be fit with a statistical
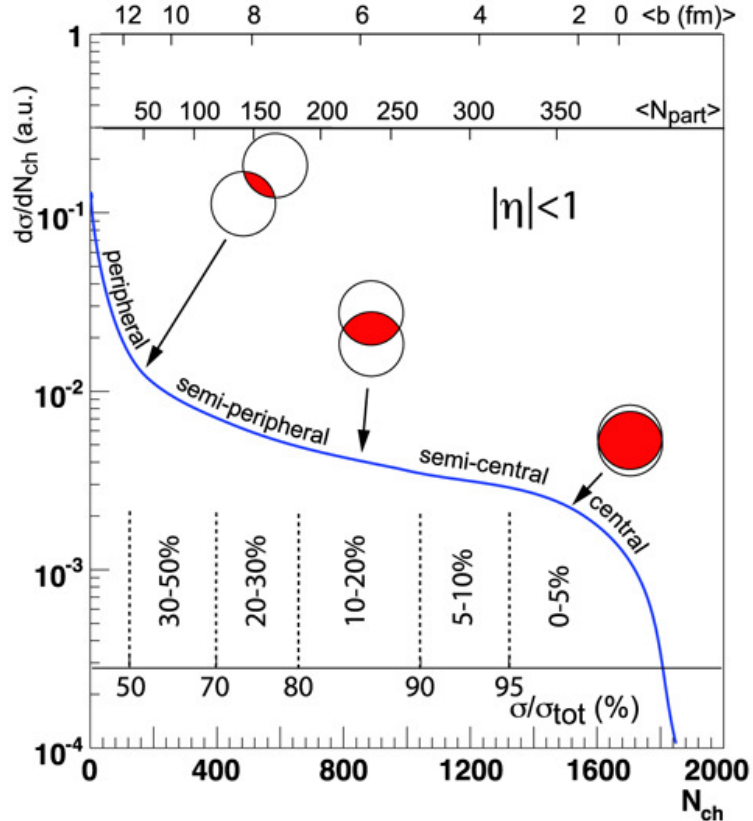
Figure 1.1 : A schematic view of the total charged particle multiplicities and their use to infer the event centrality. Figure taken from [4].

hadronization model [5] to determine the values of several thermodynamic parameters appropriate for that sample of events. The statistical hadronization model has two main free parameters [6]: the baryochemical potential, μ_B, and the temperature, T. The baryochemical potential is the derivative of the free energy with respect to the number of nucleons, which is effectively the energy cost of adding a nucleon. The temperature is a measure of the local thermal energy and is measured in MeV, where one MeV is 1.16×10^{10} degrees Kelvin.

The extent to which thermal and chemical equilibrium, an assumption in this model, is valid can be judged by comparing the ratios of the identified-particle mul-
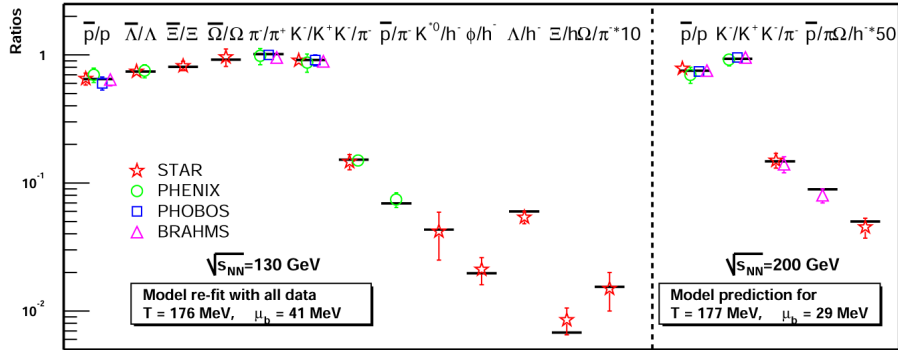
Figure 1.2 : Comparison of the experimental data for a number of different particle multiplicity ratios collected by four different experiments at RHIC at beam energies ($\sqrt{s_{NN}}$) of 130 and 200 GeV with statistical hadronization model calculations. This figure is from Ref. [7].

tiplicities to the statistical hadronization model predictions for the best fit values of (μ_B, T). Fig. 1.2 shows the comparison of experimentally measured multiplicity ratios (top of figure) from four different RHIC experiments to the statistical-model predictions. The solid black lines show the statistical model fit to all the particle ratios at a specific beam energy. The different particle multiplicity ratios are well described by the model over many orders of magnitude. The extracted temperature and baryochemical potential determined by fitting these ratios are: $\langle T \rangle$=176 MeV and $\langle \mu_B \rangle$=41 MeV at $\sqrt{s_{NN}}$=130 GeV; $\langle T \rangle$=177 MeV and $\langle \mu_B \rangle$=29 MeV at $\sqrt{s_{NN}}$=200 GeV.

This procedure can be done at any centrality and at any beam energy [9]. Shown in Fig. 1.3 are the extracted (μ_B, T) values from data at beam energies ranging from a few GeV (lower right, GSI[†]) to hundreds of GeV (upper left, RHIC). As the beam energy increases, $\langle \mu_B \rangle$ approaches zero. The temperature gradually increases as the

[†]Gesellschaft für Schwerionenforschung, Darmstadt, Germany
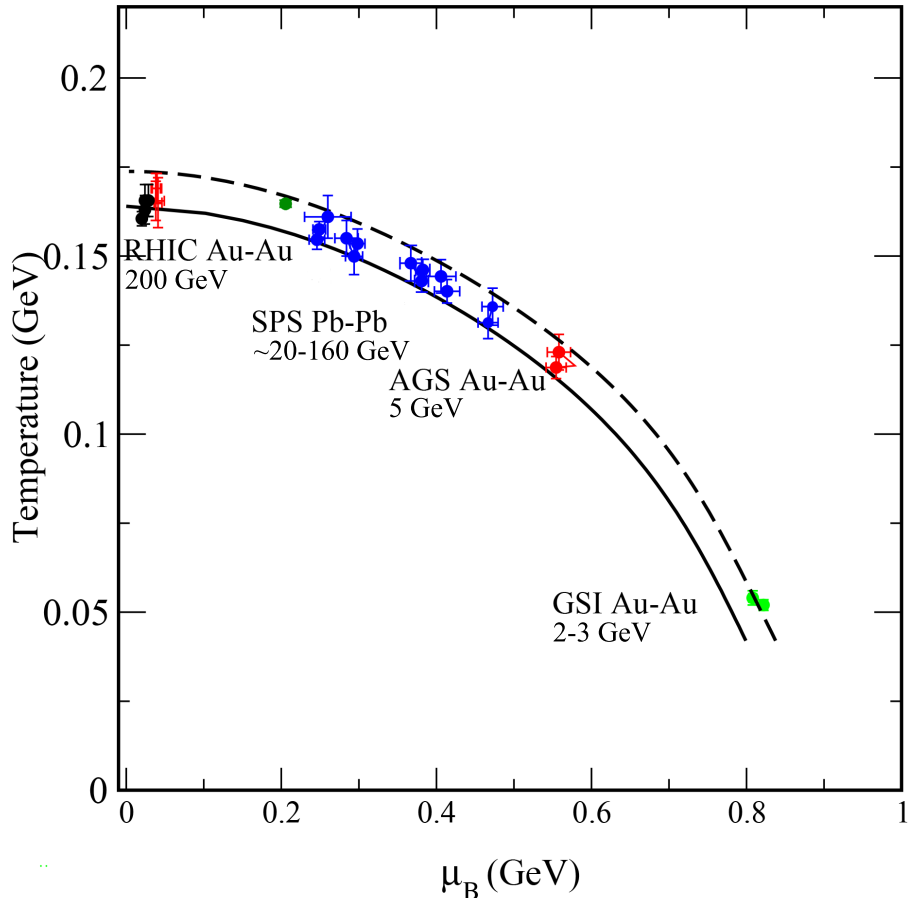
Figure 1.3 : The mean values of the temperature, T, and the baryochemical potential, μ_B, extracted from the measured particle multiplicities in heavy-ion collisions over a wide range of beam energies. Figure taken from Ref. [8].

beam energy increases.

1.1.3 Statistical moments and cumulants of identified-particle multiplicities

In previous subsections (Sec. 1.1.1 and Sec. 1.1.2), the total particle multiplicity was shown to be indicative of the collision centrality, and the average values of the identified-particle multiplicities were shown to be indicative of the thermodynamic

variables μ_B and T. In addition to the integral and average value, the shape of the multiplicity distributions in narrow centrality bins also provides insight into the properties of hot and dense nuclear matter. The shape of a multiplicity distribution is characterized by its statistical moments.
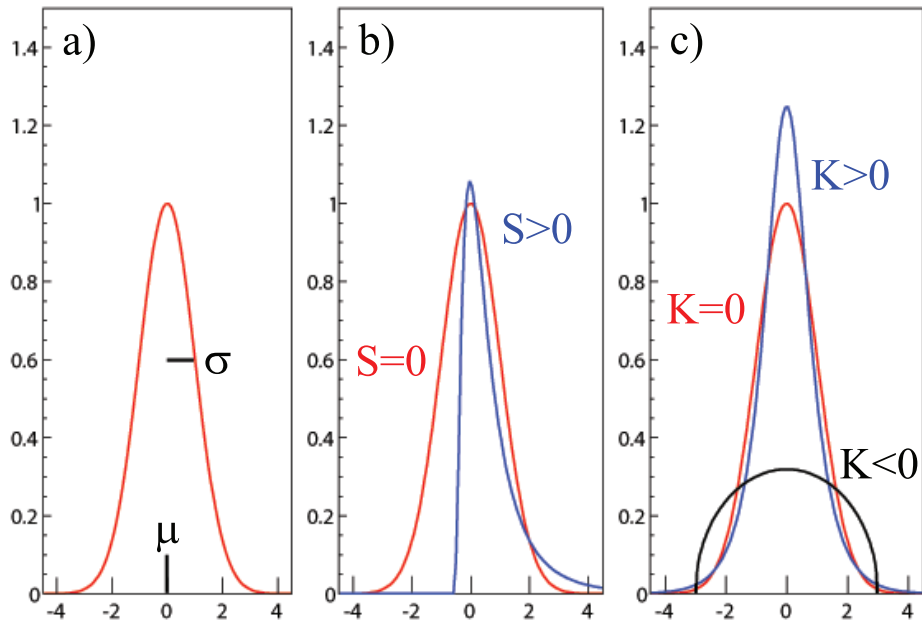
Figure 1.4 : Graphs depicting the different statistical moments of a distribution. Panel a) shows the mean (μ) and standard deviation (σ) of a Gaussian distribution. Panel b) compares the skewness (S) of two different distributions. Panel c) compares the kurtosis (K) of three different distributions.

Figure 1.4 will be used to describe the meaning of the lowest four statistical moments. For reference, the red curve in all three panels of Fig. 1.4 is the same Gaussian distribution. The zeroth moment of a distribution is the integral. The first moment is the mean, μ, which is marked in panel a) of the figure. The second moment is the variance, σ^2, which describes the width of the distribution. The square root of the variance is the standard deviation, σ, which is shown in panel a) for the Gaussian distribution. The third moment is the skewness, S, which describes the asymmetry of

the distribution. As shown in panel b), S=0 for a (symmetric) Gaussian distribution. Shown in blue in panel b) is a log-normal distribution. This log-normal distribution has a positive skewness since the bulk of the values lie to the right of the mean. A negative skewness would indicate that the bulk of the values lie to the left of the mean. The fourth moment is the kurtosis, K, which describes the "peakedness" of the distribution. A Gaussian distribution has a kurtosis of zero. Shown in blue in frame c) is a hyperbolic secant distribution, which is more peaked than a Gaussian and thus has a kurtosis greater than zero. Distributions less peaked than a Gaussian have a negative kurtosis, such as the scaled Wigner semicircle distribution shown in black.

These moments are calculated for experimentally measured particle multiplicity distributions as follows. With N denoting the number of particles in a single event, the value of the deviate in that event is defined as

$$\delta N = N - \langle N \rangle, \tag{1.1}$$

where $\langle N \rangle$ is the average number of particles over many events. The so-called cumulants of order x, κ_x, are defined using the deviates as follows:

$$\kappa_1 = \langle N \rangle, \tag{1.2}$$

$$\kappa_2 = \langle (\delta N)^2 \rangle, \tag{1.3}$$

$$\kappa_3 = \langle (\delta N)^3 \rangle, \tag{1.4}$$

and

$$\kappa_4 = \langle (\delta N)^4 \rangle - 3\langle (\delta N)^2 \rangle^2. \tag{1.5}$$

The angle brackets in these equations denote the average of the enclosed quantity. Using the cumulants, the variance, σ^2, the skewness, S, and kurtosis, K, are calculated

as

$$\sigma^2 = \kappa_2, \qquad S = \frac{\kappa_3}{\kappa_2^{3/2}}, \text{ and} \qquad K = \frac{\kappa_4}{\kappa_2^2}. \qquad (1.6)$$

Additionally, one can express certain moments products, such as $K\sigma^2$ and $S\sigma$, in terms of the ratios of the cumulants:

$$S\sigma = \frac{\kappa_3}{\kappa_2}, \text{ and} \qquad K\sigma^2 = \frac{\kappa_4}{\kappa_2}. \qquad (1.7)$$

1.1.4 Summary

Each of the topics described in Sec. 1.1 are key components of this thesis, which describes the search for a possible critical point in nuclear matter. The hottest and densest nuclear systems are formed in central collisions, which must be selected carefully. Using samples of central collisions, statistical hadronization models infer the average temperature and baryochemical potential appropriate for that sample of events. These quantities, T and μ_B, are in fact the axes of the phase diagram of nuclear matter. The statistical moments of the multiplicity distributions described in Sec. 1.1.3 are the experimental observables that could be sensitive to the QGP-hadron transition and the critical point.

1.2 Phase diagram of nuclear matter with a possible critical point

A phase diagram shows the physical states of a substance under different thermodynamic conditions. For example, the phase diagram of water as a function of pressure and temperature has specific regions for ice, water, and vapor. The triple point in water is the pressure (6.1173 mbar) and temperature (273.16 °K) at which the phases

are indistinguishable. For nuclear matter, the axes of the phase diagram are the temperature and baryochemical potential, which were discussed in Sec. 1.1.2. The boundaries in such a phase diagram are largely speculative. Also, it is not clear if a critical point in nuclear matter phase diagram exists.

1.2.1 Nuclear phase diagram

Various models make predictions about the boundaries of the nuclear phase diagram. However, these predictions are largely speculative. Fig. 1.5 shows a schematic view of
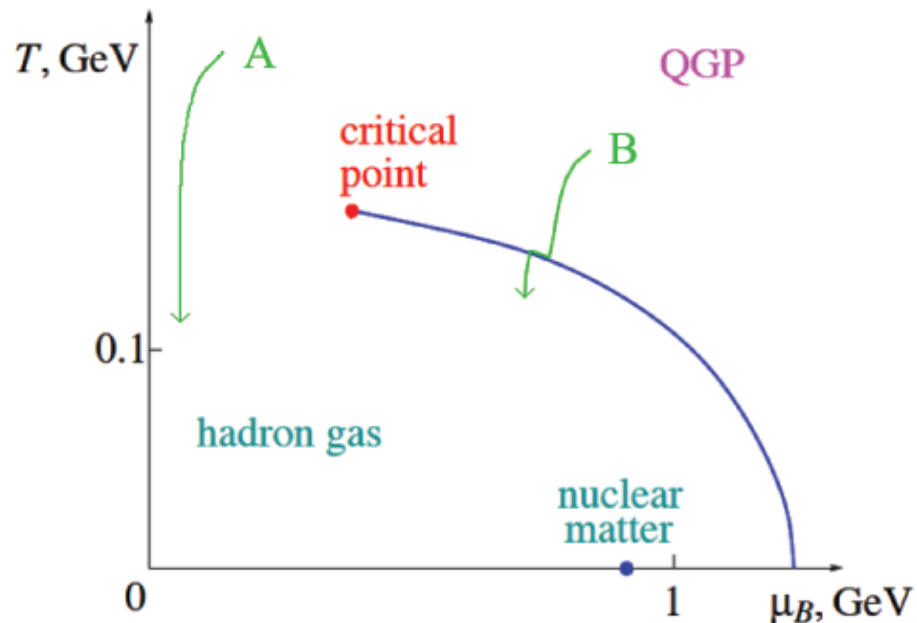
Figure 1.5 : Phase diagram of nuclear matter, with temperature on the y-axis and baryochemical potential on the x-axis. A first-order phase transition is shown as a blue line. Lines "A" and "B" show two possible trajectories taken by a of a hot and dense nuclear system during its evolution following a heavy-ion collision.

the phase diagram of nuclear matter [10]. The temperature is on the y-axis and the baryochemical potential, μ_B, is on the x-axis. Theory and experiment suggest that

there should be distinct regions in this phase diagram. All "normal" matter sits in the blue point labeled as nuclear matter, at a temperature of zero and a value of μ_B at the nucleon mass of $\sim$940 MeV.

Nuclear collisions generally proceed as follows. Early hard nucleon-nucleon collisions create "hot spots," producing many secondary particles. Most of the initial compression and particle production occurs early in the collision, at times on the order of 1 fm/c. It is at this point that the system is in some sort of local equilibrium, and can thus be placed somewhere in Fig. 1.5. At facilities with "low" beam energies (GSI, AGS[‡], SPS[§]) the system starts near the letter "B" in Fig. 1.5; at the highest beam energies at RHIC, the system starts near the letter "A" in this figure. The system then evolves, in general, hydrodynamically and expands and cools along the trajectories depicted as green arrows in the figure. The point at which particle production ceases is called chemical freezeout. RHIC was the first collider capable of beam energies high enough that the system of nuclear matter evolved along the steep vertical trajectory near the y-axis in the phase diagram, transitioning during cooling from a QGP to a hadron gas. This transition from a QGP to a hadron gas at low values of μ_B is a "crossover" transition, in which all thermodynamic parameters vary smoothly without discontinuities. This crossover-transition region near values of $\mu_B\sim$0 is expected from lattice Quantum Chromodynamics (QCD) calculations [11] and is seen in the data [12].

The blue line in Fig. 1.5 shows the expectation that at high values of μ_B, the boundary between the QGP and hadron gas phases is a first-order transition. This is

---

[‡]Alternating Gradient Synchrotron, Brookhaven National Laboratory (BNL), Upton, NY

[§]Super Proton Synchrotron, Organisation européenne pour la recherche nucléaire (CERN), near Geneva, Switzerland

implied by various theories [10]. Path "B" in Fig. 1.5 shows how a system that crosses the posited first-order phase transition would evolve. The system would cool until it hit the first-order phase transition, progress to the left along the phase-transition line due to the latent heat, then cool again in the hadronic phase.

If there is indeed such a first-order phase transition, there should be a critical point at the low-μ_B end of the first-order phase-transition line. The discovery of the critical point would be a signpost measurement, instantly transforming the knowledge of the phase diagram from largely speculative to experimental fact.

Two aspects of theory and models are now relevant: the susceptibility and the correlation length. The former may reflect QGP-to-hadronic-matter transitional behavior, while the latter may reflect the critical point. Each is described in turn in the following two subsections.

1.2.2 Susceptibilities of conserved quantities and their ratios

An order parameter is a quantity that has distinctly different values in different phases. For the liquid/gas phase transition of water, the order parameter is the density. The QCD order parameter used to define the phases of nuclear matter are the thermodynamic susceptibilities, χ, of conserved quantities such as electric charge (Q), baryon number (B), and strangeness (S). The susceptibility is the derivative of the logarithm of the QCD partition function Z (i.e., the pressure):

$$\chi_{Q,B,S} = \frac{1}{VT^3}(\partial^2 logZ/\partial\mu_{Q,B,S}), \tag{1.8}$$

where V is the volume and T is the temperature. The QCD conserved quantities Q, B, and S are referred to simply as "charges." These charges have deviates

$$\delta N_X = N_X - \langle N_X \rangle, \tag{1.9}$$

where X = B, Q, or S. The quadratic, cubic, and quartic charge fluctuations can then be defined using the moments of the deviates [13]:

$$\chi_2^X = \frac{1}{VT^3}\langle N_X^2 \rangle, \tag{1.10}$$

$$\chi_3^X = \frac{1}{VT^3}\langle N_X^3 \rangle, \tag{1.11}$$

and

$$\chi_4^X = \frac{1}{VT^3}(\langle N_X^4 \rangle - 3\langle N_X^2 \rangle^2). \tag{1.12}$$

The relationship between the susceptibilities of conserved charges and the moments of the charge distributions is very similar to the relationship between the cumulants and the moments of multiplicity distributions described in Sec. 1.1.3. In fact, the ratios of the susceptibilities are directly related to the cumulants of the multiplicity distributions via

$$\frac{\chi_3}{\chi_2} = \frac{\kappa_3}{\kappa_2} = S\sigma, \tag{1.13}$$

and

$$\frac{\chi_4}{\chi_2} = \frac{\kappa_4}{\kappa_2} = K\sigma^2. \tag{1.14}$$

The cumulants thus directly link the susceptibilities in lattice QCD to experimentally measurable moments of particle multiplicity distributions. Also, the volume and temperature dependence in Eqs. 1.10-1.12 drops out of these ratios.

Lattice theory predictions

The electric charge, strangeness, and baryon number susceptibilities should have distinctly different values in the QGP and hadronic phases [13]. Also, localized enhancements of the electric charge, strangeness, and baryon number susceptibility ratios may be indicative of a critical point [14]. Shown in Fig. 1.6 is the ratio of the fourth to the

second order cumulants of the conserved quantities versus the temperature obtained from lattice QCD calculations [13]. The quartic to quadratic baryon number susceptibility ratio is shown on the left, the strangeness susceptibility ratio is shown in the middle, and the electric charge susceptibility ratio is shown on the right. Shown in different colors are different lattice spacings.¶ The Hadron Resonance Gas (HRG) expectation is shown in black on the left side of the figures. The HRG will be discussed in a subsequent chapter, but it is effectively the expectation for hadronic matter. The Stefan-Boltzman (SB) gas expectation is shown in black on the right side of the figures. The SB expectation is the value of the susceptibility ratios in an ideal free quark gas, and thus represents the QGP. The distinctly different values of the HRG and SB expectations of the susceptibility ratios reflects the applicability of the susceptibilities as an order parameter for nuclear matter. These conserved quantities can show a temperature-localized peak, which is indicative of a possible critical point [14]. These quantities also show a drop in values from the HRG expectation at low energies to the SB expectation at higher energies, which is indicative of a phase transition. To the
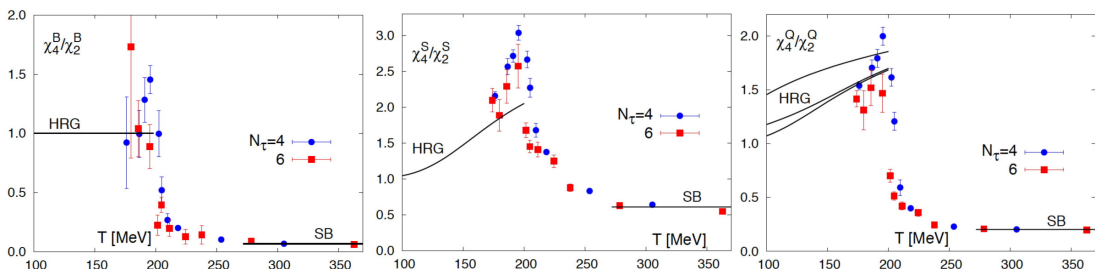
Figure 1.6 : The ratio of the fourth to the second order cumulants of baryon number (left), strangeness (middle), and electric charge (right) fluctuations as calculated by the RBC-Bielefeld collaboration lattice theory group [13]. Different size lattices are shown in different colors. The lines marked HRG and SB are the limiting behavior for hadronic matter and the QGP, respectively (see text).

¶Lattice calculations become increasingly more CPU time intensive as the lattice size increases.

extent that one can measure the multiplicity distributions of the conserved quantities of baryon number, charge, and strangeness, one may find changes in the values of the moments products Sσ and Kσ^2 as a result of the QGP to hadronic matter transition and possibly the critical point.

Numerous models [15–24] and lattice theories [25–27] predict a critical point at μ_B>0. Fig. 1.7 shows the QCD phase diagram with phenomenological model (black) and lattice QCD (green) predictions of the location of the critical point [14]. There is clearly no theoretical consensus on the location of the critical point among the theoretical approaches that predict that the CP exists. This may be related to the numerical difficulties, and the different numerical methods used to overcome these difficulties, in the very computer-intensive lattice calculations. While there is little consensus, it remains true that a number of different theoretical approaches feature a CP. The question of the existence of the CP, and the measurement of its location in the phase diagram, is thus perhaps best answered experimentally.

However, not all lattice theories predict the existence of a critical point [28–30]. Fig. 1.8 shows two possible scenarios of the phase diagram of nuclear matter. The left panel shows a QCD phase diagram very similar to Fig. 1.5, where there is a first-order transition and a critical point between the QGP and hadron gas phases at μ_B>0. The right panel shows a QCD phase diagram where the transition between the QGP and hadron gas weakens, resulting in a crossover at even very large values of μ_B, and there is no critical point.

The speculative nature of the phase diagram of nuclear matter, as well as the wide range of theoretical predictions concerning the nature of the phase transition, provides experimentalists with the opportunity to provide insight using experimental data.
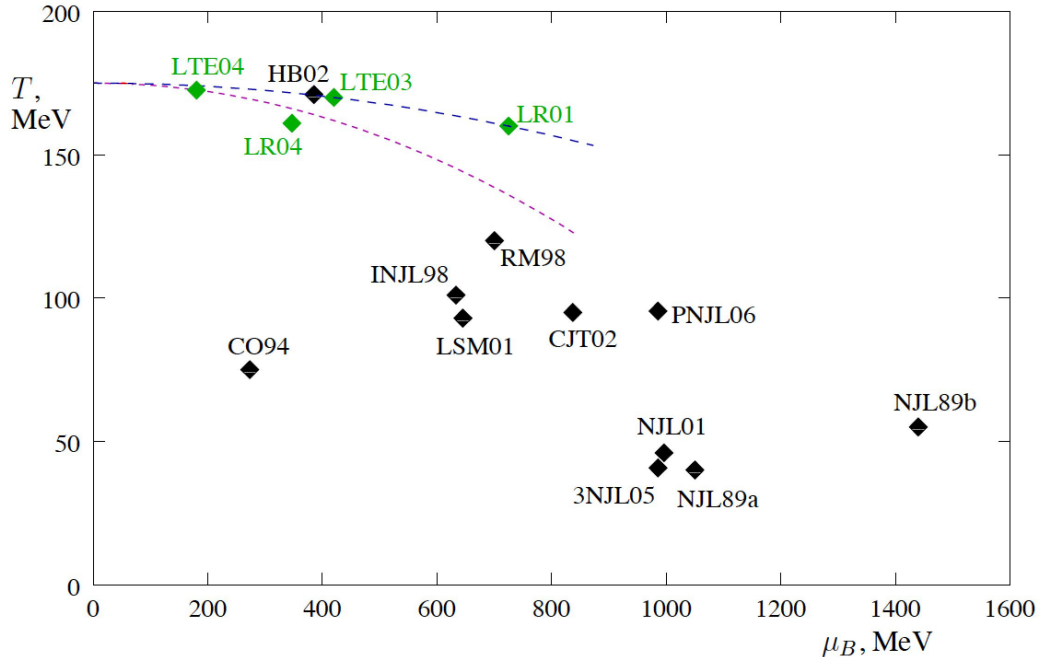
Figure 1.7 : A schematic representation of the QCD phase diagram, with temperature on the y-axis and baryochemical potential on the x-axis. Shown in black are various model predictions for the location of the QCD critical point. Shown in green are predictions from lattice QCD. See Ref. [14].

1.2.3 Correlation length

In Sec. 1.2.1, the susceptibilities of conserved quantities are directly calculable in theory and may, as an order parameter, be indicative of a transition between the hadron gas and the QGP phases. Also relevant for the study of the phase diagram is a signal directly related to the presence of the critical point. This signal could potentially result from the phenomenon known as critical opalescence.

Critical opalescence was originally observed in 1869 when a flask of liquid CO_2 at a specific pressure became cloudy as the temperature increased [31]. This cloudiness was indicative of density fluctuations that formed phase-specific domains that were large compared to the wavelength of visible light. This resulted in the substance becoming
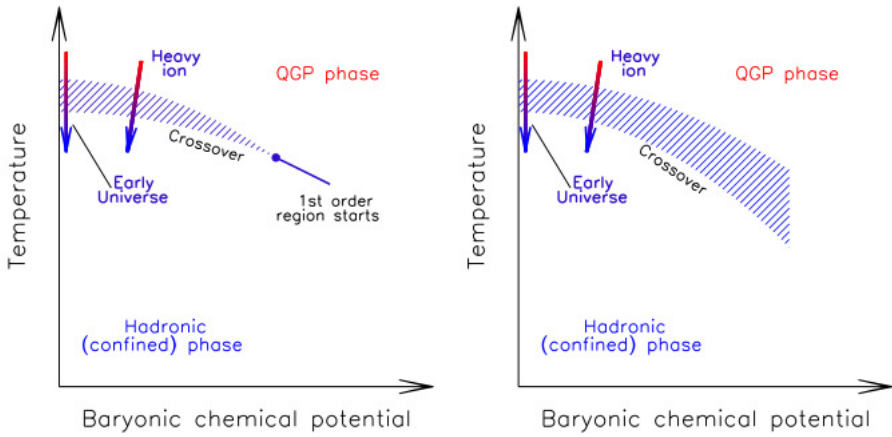
Figure 1.8 : Two possible QCD phase diagrams from Ref. [28]. In the left frame, the transition between the QGP and the hadron gas phases grows stronger and turns into a first-order phase transition with a terminal critical point. In the right frame, the transition between the QGP and the hadron gas phases weakens and there is no critical point.

cloudy as the temperature approached the critical temperature. This phenomenon was explained theoretically forty years later by Albert Einstein [32]. These long-range density correlations are characterized by the "correlation length," ξ. A general feature of critical points in various substances is the divergence of the correlation length [33].

Such an effect may also exist in the nuclear systems created at RHIC. If the nuclear systems formed at a specific beam energy and centrality freeze out close to the critical point, critical opalescence could occur in those systems, resulting in long-range density fluctuations. The correlation length has a value of $\xi \sim 0.5$-1 fm in "normal" nuclear matter and could be as large as $\xi \sim 2$-3 fm near the critical point [34].

The non-linear sigma model (NLSM) is a phenomenological approach allowing the study of critical opalescence in nuclear systems. In this model, the correlation length is directly related [10, 35, 36] to the cumulants of the multiplicity distributions,

$$\kappa_2 \propto \xi^2, \qquad \kappa_3 \propto \xi^{9/2}, \text{ and } \qquad \kappa_4 \propto \xi^7. \tag{1.15}$$

Likewise, the correlation length is directly related to the moments products:

$$S\sigma = \frac{\kappa_3}{\kappa_2} \propto \xi^{5/2}, \text{ and} \tag{1.16}$$

$$K\sigma^2 = \frac{\kappa_4}{\kappa_2} \propto \xi^5. \tag{1.17}$$

Therefore, larger orders of the moments products have a stronger dependence on the correlation length. A beam-energy-localized or centrality-localized divergence of the moments products $S\sigma$ and $K\sigma^2$ might thus reflect the phenomenon of critical opalescence, signaling the critical point.

In the NLSM with reasonable input parameters, a prediction [35] can be made of the magnitude of the expected enhancement of the moments products in the presence of the critical point. Assuming a critical baryochemical potential of 400 MeV and a maximum correlation length of 2 fm, the critical contribution to the moments products can be parameterized using universality arguments. The width in μ_B of the critical enhancement, Δ, is assumed to be between 50 and 200 MeV, with $\sim$100 MeV as the value implied by lattice calculations [37].

Fig. 1.9 shows the expected dependence of ω_4 of protons ($\sim K\sigma^2$) versus μ_B. The quantity ω_4 is

$$\omega_4 = \frac{\kappa_4}{\langle N_p + N_{\bar{p}} \rangle}, \tag{1.18}$$

and is related to the moments product $K\sigma^2$ via

$$K\sigma^2 = \frac{\omega_4 \langle N_p + N_{\bar{p}} \rangle}{\kappa_2}. \tag{1.19}$$

Near the assumed location of the critical point, there is a localized enhancement of ω_4 of order $\sim$400 in this model. Since the NLSM is "isospin-blind," total moments (i.e., $N_p + N_{\bar{p}}$) should be as or more sensitive to the critical point than net moments (i.e., $N_p - N_{\bar{p}}$). The inset on the left side of the figure shows the Poisson expectation of unity, which is the expected value of ω_4 in the absence of critical fluctuations.
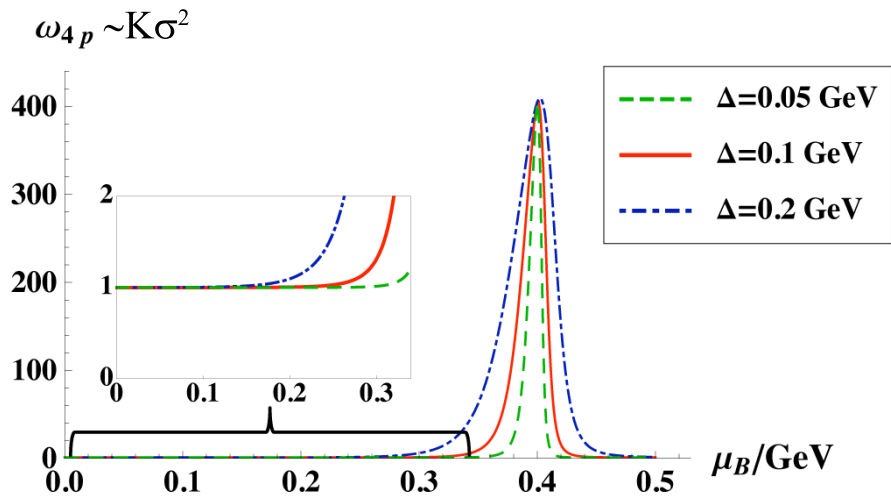
Figure 1.9 : The expected dependence of the fourth moment ω_4 of protons as a function of the baryochemical potential. A critical baryochemical potential at 400 MeV is assumed. The width in μ_B of the critical enhancement is Δ. Figure taken from Ref. [35].

The parameters in the NLSM are not well known, but this approach suggests that the CP may result in sharp increases in the fourth moment products. Depending on the specific values of the poorly known NLSM parameters, different particle groups may be the most sensitive to the CP, so it is important to study many different particle groups experimentally.

In a follow-up paper to Ref. [35], Stephanov [36] further refined the NLSM. A parameter that was previously simply taken to be of order one was found to remain

small but undergo a μ_B-dependent sign change. This refinement resulted in a slight change in the shape of the critical enhancement shown in Fig. 1.9. The NLSM still predicted a large enhancement at the critical point, but now also predicted a very slight negative contribution on the low-μ_B side of this large peak. This negative contribution would be expected to result in moments values that are below the non-critical (Poisson) baseline just next to the large enhancement at slightly larger μ_B values.

1.2.4   Summary

The susceptibilities of conserved quantities are directly calculable in lattice theory and are indicative of transitional behavior between a hadron gas and a QGP. These susceptibilities are mathematically related to the experimentally accessible moments of multiplicity distributions. According to the NLSM, the correlation length is also related to the moments of the multiplicity distributions and should diverge near the critical point. Thus, two very different approaches, lattice models and the NLSM, both indicate that the moments of the multiplicity distributions provide a tool for the experimental exploration of the phase diagram of nuclear matter and the search for a possible critical point.

1.3   Experimental approach

This thesis will describe the study of the lowest four moments of the multiplicity distributions of identified particles in Au+Au collisions at STAR to search for divergences of the susceptibilities or correlation lengths. Net-protons (protons minus antiprotons) will be used as a proxy of baryon number, net-Kaons (K^+-K^-) will be used as a proxy of strangeness, and net-charge (positive minus negative) will be used

as a proxy of electric charge. Also studied are total-protons (protons plus antiprotons), since the NSLM is isospin-blind and suggests that the moments of total-protons may be the strongest signal of critical behavior [35].

In both the lattice calculation and the NLSM, the magnitude of the divergence may depend on the specific particles considered. It is thus important to carefully study many different particle groups.

The experimental acceptance is also generally different for different particles. It was pointed out in Ref. [38] that the experimental acceptance can have a dramatic effect on the sensitivity of such moments analyses to critical behavior. Basically, the sensitivity of an experiment to such critical behavior scales with the third and fourth power of the binomial parameter, p, for the skewness and kurtosis, respectively. The parameter, p, is effectively the overall efficiency of the experiment for measuring the particle relative to a full 4π perfect detector. As this parameter approaches zero, the critical contribution to the moments values is strongly suppressed, and all measured moments will simply be Poisson-like, even in the presence of the CP. This parameter includes both the experimental geometrical acceptance and the inefficiencies resulting from the offline cuts on the tracks allowed to be counted in a multiplicity distribution. Even in STAR's wide acceptance, p ranges from 1/10 to 1/5.

As will be described in the next chapter, the kaon and proton particle groups involve cuts to perform the particle identification (PID). This makes the net-charge observables attractive, as the values of p should be larger for net-charge than they are for any multiplicity distribution following PID cuts. The Time-of-Flight system, also described in the next chapter, makes two important positive contributions as well. It reduces contamination in the particle identification, and it dramatically increases the momentum range over which particles can be directly identified. This increases the

value of the binomial parameter p and increases the sensitivity to critical behavior.

Chapter 2

Experimental setup and analysis method

2.1   Relativistic Heavy Ion Collider (RHIC)

RHIC is a particle accelerator capable of colliding heavy ions and polarized protons
and is located at Brookhaven National Laboratory (BNL) in Upton, New York. Shown
in Fig. 2.1 is an aerial view of RHIC. The RHIC ring is 1.2 km in diameter. Shown in
red in the figure is the beam path. Three different accelerators in the injection chain
increase the energy of the colliding species and strip electrons from heavy ions. Heavy-
ion beams begin in the Tandem Van de Graaff accelerator (TANDEMS). The ions then
reach the Alternating Gradient Synchrotron (AGS), where the last of the electrons are
stripped away. From there, the heavy ions are delivered to the RHIC storage ring [39].
As the ions enter the RHIC ring, they are separated into two different beams traveling
in opposite directions around the ring. The RHIC is capable of colliding polarized
protons up to 510 GeV and nuclei from ∼5 to 200 GeV/nucleon. The beams can
collide at one of six possible interaction regions. The experiment located at the 6
o'clock position on the RHIC ring, the Solenoidal Tracker at RHIC (STAR), provided
the data used here.

2.2   Solenoidal Tracker at RHIC (STAR)

Shown in Fig. 2.2 is a cutaway view of the STAR detector. STAR azimuthally sur-
rounds the collision region. STAR weighs over 1200 tons and is over three stories
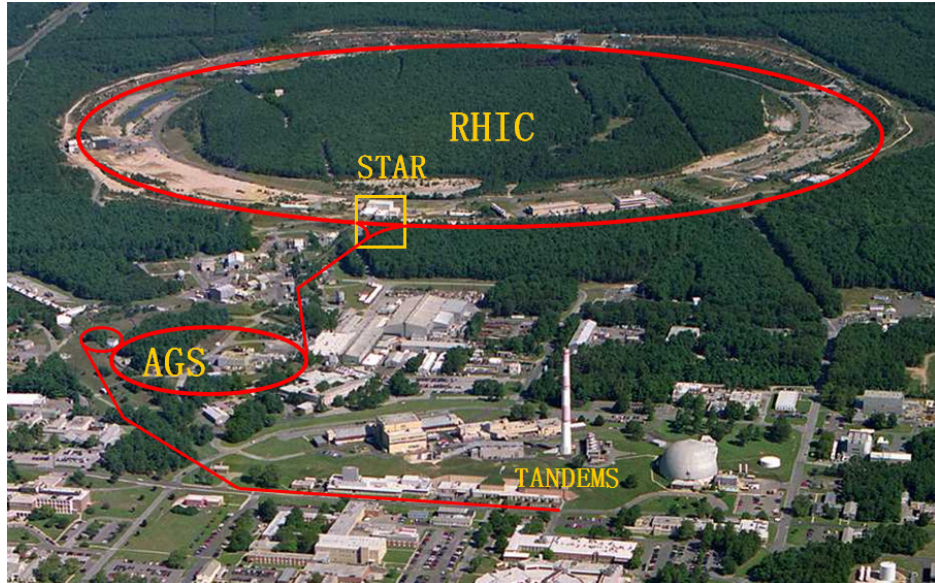
Figure 2.1 : A schematic of the different stages of the RHIC accelerators at BNL. The STAR experimental hall collision point is also shown.

tall. The beam line is shown as a green line in this figure. The magnet is 6.85 m in length and generates a magnetic field along the beam direction of 0.5 Tesla. Labeled in yellow are the primary detectors for the present analysis. These include the Time Projection Chamber (TPC), the Time of Flight (TOF) detector, and the Vertex Position Detector (upVPD).

2.2.1   The Time Projection Chamber (TPC)

The main tracking detector at STAR is the Time Projection Chamber (TPC) [41]. The TPC is a gas-filled cylinder that is ∼4 m in diameter and ∼4 m long, as shown in Fig. 2.3. The TPC is inside the STAR magnetic field. The beam pipe passes through the center of the TPC at ∼(x=y=0)* in Fig. 2.3. The TPC provides a full azimuthal

---

*In the STAR coordinate system, the z-axis points west along the beam line, the x-axis points south, and the y-axis points upward. The origin is at the geometric center of STAR inside the beam
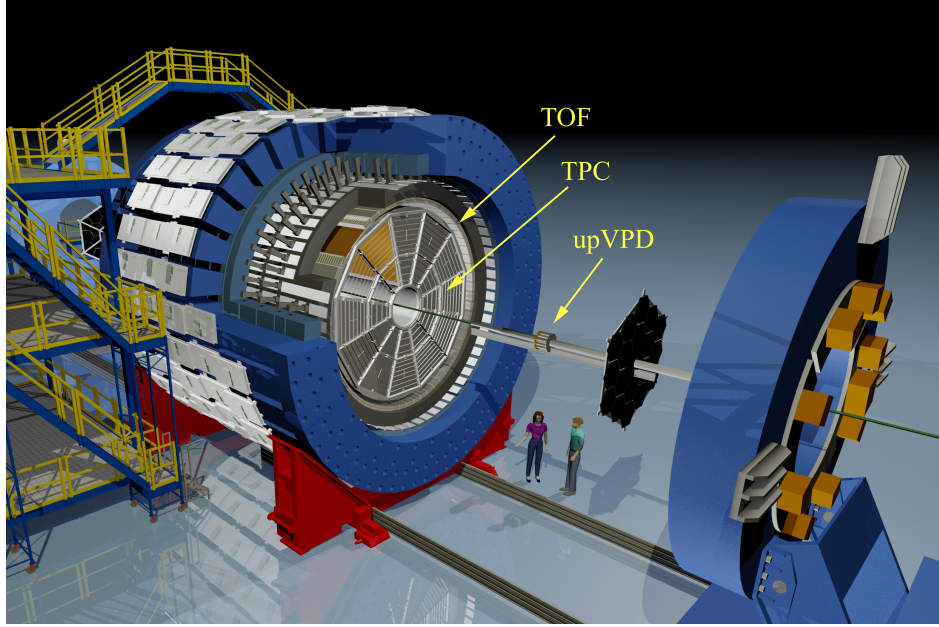
Figure 2.2 : A cutaway view of the STAR experiment. Labeled in yellow are the primary subsystems for this analysis, which include the Time-of-Flight (TOF) detector, Time Projection Chamber (TPC), and Vertex Position Detector (upVPD). Figure taken from Ref. [40].

coverage $(0<\phi<2\pi)$. The coverage along the z-direction of Fig. 2.3 is given in units of pseudorapidity, η, defined as:

$$\eta = -\ln(\tan\frac{\theta}{2}). \tag{2.1}$$

The TPC covers a pseudorapidity range of -1<η<1 (45<θ<135 with respect to the beam line). The TPC is divided into two parts by the central membrane shown at z=0 in Fig. 2.3. Each half is subdivided azimuthally into 12 sectors, each with an inner and outer section. There are a total of 136,608 readout pads in the TPC system.

The TPC measures the tracks from charged particles and gives their momentum, p (GeV/c), path length, s (cm), and the ionization energy loss, dE/dx (MeV/cm), in

---

pipe.
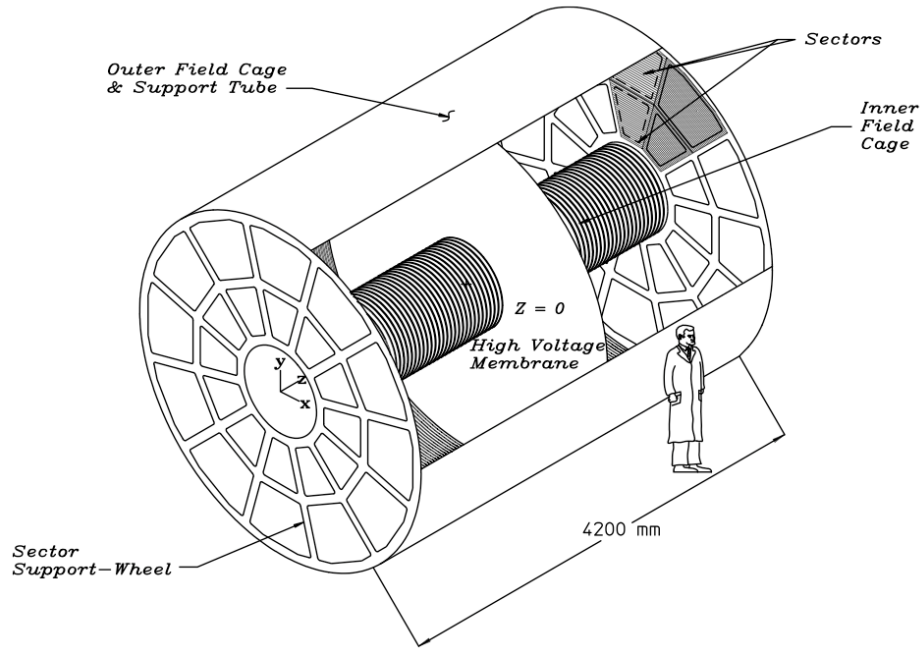
Figure 2.3 : A schematic view of the Time Projection Chamber (TPC).

the TPC gas. The dE/dx information is used for particle identification (PID). The amount of energy lost by different particles depends on the charge and mass of the particles. The ionization energy "clusters" in the TPC thus provide information useful for identifying the species of a given track. With this information, one can directly identify pions, Kaons, and protons in a momentum range from 0.1 to 0.7 GeV/c. Protons can be directly identified, versus pions plus Kaons, up to ~1.0 GeV/c.

Track and vertex reconstruction

Tracks within the TPC are reconstructed using tracking software. There are thousands of readout pads in the TPC that register hits in time buckets along pad rows during an event. The software looks for series of measured hits that can be associ-

ated to form a helical track. This track is referred to as a global track. Once such a track is formed, the software associates physical information, such as the angle and momentum components, and track-reconstruction quality information with the track.

Once the global tracks are reconstructed, their trajectories are extrapolated to the beam axis. Vertex reconstruction software looks for locations along the beam line from which global tracks appear to originate, and labels these locations as primary vertices. The vertices are then ranked, and the highest-ranked vertex is used in analyses. Any global tracks that have a distance of closest approach (DCA) of less than 3 cm to this primary vertex are flagged as primary tracks. These have the collision vertex added as a high-precision first space point in the track, and are then refit to improve the momentum and trajectory information.

The physical information associated with a track includes the momentum, path length, and dE/dx. The quality information includes the number of hits assigned to the track, the number of hits possible for that trajectory through the TPC, and the number of hits used in the dE/dx calculation. These quantities are used to select high-quality tracks for physics analysis. Standard track cuts at STAR were implemented in this analysis to select good primary tracks. Only tracks that had at least 15 hits out of a possible 45 were used. At least 10 hits were required for the dE/dx calculation. The ratio of the number of reconstructed hits to the number of hits possible was required to be greater than 0.52 to avoid so-called "split tracks." A cut on the maximum DCA of 1 cm was made to ensure only particles created in the collision, and not particles resulting from weak decays, were counted.

2.2.2 The Time-of-Flight Detector (TOF)

The TPC provides the tracking information, but its direct PID capabilities are limited to low values of the particle momenta. The STAR Time-of-flight (TOF) detector significantly extends the PID capabilities, identifying charged hadrons up to a maximum momenta $\sim$3 times greater than that possible from the TPC alone [42]. The TOF system directly surrounds the outer cylinder of the TPC, as can be seen in Fig. 2.2. It also provides full azimuthal coverage ($0<\phi<2\pi$), and covers a pseudorapidity range of -0.94$<\eta<$0.94.

The TOF system measures "stop" times relative to the start time measured by the Vertex Position Detector (VPD). This detector is located in the very forward direction ($4.43<|\eta|<5.1$) on the east and west sides of STAR, as shown in Fig. 2.2 [43]. The VPD uses phototubes and a Pb converter to detect photons that travel very close to the beam pipe following a collision. The time at which the photons reach each start detector are calculated as:

$$\text{t}_{\text{east}} = t_0 + \frac{L + z_{vertex}}{c} \qquad \text{t}_{\text{west}} = t_0 + \frac{L - z_{vertex}}{c}, \qquad (2.2)$$

where t_0 is the actual time of the collision, L is the distance to the VPD from the center of STAR, and z_{vertex} is the location of the collision vertex along the z-direction. Therefore, the VPD can measure the start time of the collision via

$$t_0 = \frac{\text{t}_{\text{east}} + \text{t}_{\text{west}}}{2} - \frac{L}{c}. \qquad (2.3)$$

The active "stop-side" detectors in the TOF system are Multigap Resistive Plate Chambers (MRPC), of which there are 3840 in total. These MRPCs are located inside trays mounted on the exterior of the TPC but still inside the STAR magnetic field. There are 120 trays positioned in two rings of 60 trays each, and each tray

holds 32 MRPC modules. Each MRPC is a stack of glass plates with 220-μm wide gaps between each plate [44], as seen in Fig. 2.4. Each MRPC has six read-out pads, or "cells" (shown in red), so the TOF system has 32040 channels in total. When a charged particle crosses an MRPC, a signal is readout on a pad, allowing a determination of the stop time using precise fast-timing electronics.
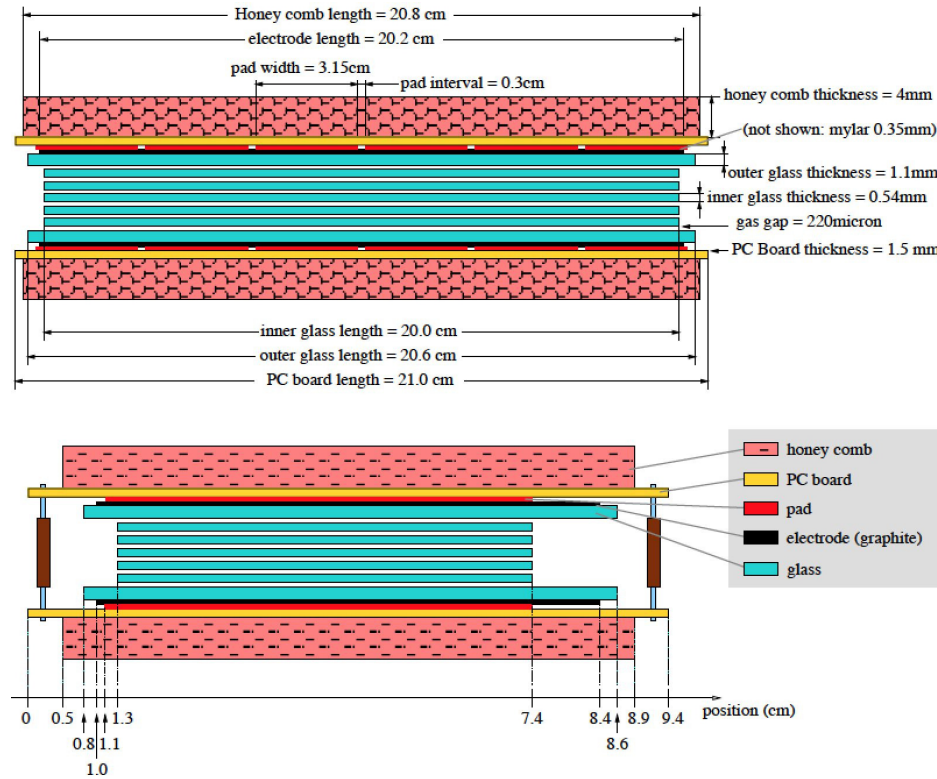
Figure 2.4 : A view of an MRPC from two different sides. The glass plates are shown in blue and the readout pads are shown in red.

A map is made of all of the TOF cells that were hit. Another map of the global tracks pointing to TOF cells is made. From these maps, lit cells struck by only one primary track are identified. The TOF timing information for that cell is thus associated with that track. The TOF software also stores quality information, such

as the number of neighboring cells that were also hit and the local y-coordinate ($\approx \phi$) of the hit on the cell.

Once one has the start time from the VPD and the stop time from the TOF trays, the time of flight, Δt, is calculated via

$$\Delta t = \mathrm{t_{stop}} - \mathrm{t_{start}}. \tag{2.4}$$

Then, using the path length, S, from the TPC, the inverse velocity, $1/\beta$, is calculated via

$$\frac{1}{\beta} = \frac{c\Delta t}{S}. \tag{2.5}$$

Using the momentum, p, of the charged particle (from the TPC), the equation $\mathrm{M}^2 = \mathrm{p}^2(1/\beta^2 - 1)$ allows the calculation of the mass-squared of the charged particle, which directly identifies the particle.

In order to get the best timing resolution possible, several calibrations have to be done to the TOF data, such as slewing corrections, geometric corrections for the location of the hit on the MRPC pad, and corrections for the integrated non-linearity (INL) of the digital chips in the electronics [45]. The INL correction is a nuance of the "HPTDC" chip used in the TOF system, and these corrections were measured before the installation of the TOF system. This was done in a test stand at Rice University for each channel of $\sim$970 electronics boards that make up the TOF system [45]. The other corrections are performed using the data itself, as described below.

Slewing is a dependence of the apparent time of a hit on the total charge of the hit. Cables and traces in electronics boards also add "offsets." These effects must be removed. Pions are selected using the TPC dE/dx information. The inverse velocity difference between the TOF-measured β and the β expected for a pion, $\frac{1}{\beta} - \frac{1}{\beta_\pi}$, is

calculated via:

$$\frac{1}{\beta_\pi} = \frac{c\Delta t_\pi}{S},$$ (2.6)

where

$$\Delta t_\pi = \frac{S}{c} * (\frac{\sqrt{m_\pi^2 + p^2}}{p}).$$ (2.7)

A plot of $\frac{1}{\beta} - \frac{1}{\beta_\pi}$ versus the "Time-over-Threshold" (ToT) is made. The ToT is the detector pulse width. These histograms are fit with splines (piecewise smooth polynomial functions), and the resulting correction functions are used in subsequent passes through the data. In these subsequent passes, the granularity of the correction is made finer, and the cuts are narrowed until the dependence is flat and centered around zero, removing the slewing effect. To address the dependence of the stop time on the location of the hit on a cell, a plot of $\frac{1}{\beta} - \frac{1}{\beta_\pi}$ versus the location of the hit in the z-coordinate direction (parallel to the beam pipe) is made. This histogram is also fit with splines, and the data is similarly flattened in subsequent passes to remove the effects of offsets.

Fig. 2.5 shows example PID plots from the TPC (left frame) and TOF (right frame). The left frame shows the TPC dE/dx versus the momentum. One can see distinct bands for pions (π), Kaons (k), protons (p), and deuterons (d). Pions and Kaons can be identified up to $\sim$0.7 GeV/c, after which the bands merge and those two particles are indistinguishable. Protons can be efficiently identified up to $\sim$1 GeV/c.

In the right frame, the values of $1/\beta$ from TOF versus the momentum are plotted. Again, different charged particle species are seen as distinct bands. Pions and Kaons can be identified up to $\sim$1.8 GeV/c. Protons can be identified up to $\sim$3 GeV/c. The TOF system extends the momentum reach of the direct PID capabilities of STAR by a factor of $\sim$3 in momentum.
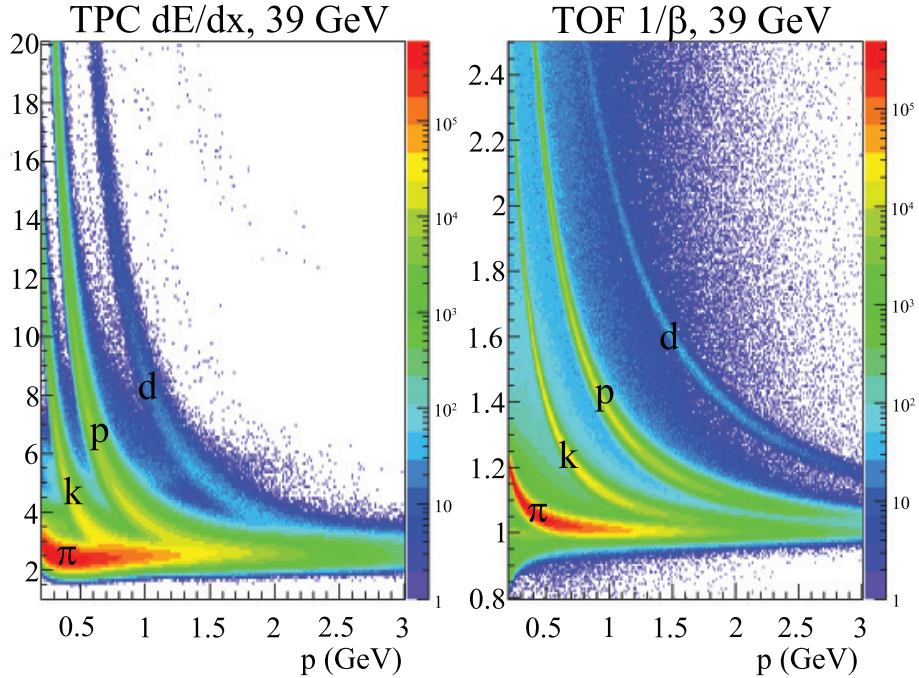
Figure 2.5 : Example PID plots from STAR. On the left side is a plot of the dE/dx versus the momentum. On the right side is a plot of $\frac{1}{\beta}$ versus the momentum. Different species of charged particles, such as pions (π), Kaons (k), protons (p), and deuterons (d), are seen as the distinct bands.

Early STAR analyses of the moments products of net-protons were done using "TPC-only PID" with the p_T selection of $0.4 < p_T < 0.8$ GeV/c [46, 47]. However, such a p_T cut allows PID contamination since particles with a momentum, p, of up to ~1 GeV/c survive the cut, and this momentum limit is close to where the TPC struggles to distinguish protons from pions and Kaons. For tracks with TOF information, the particle identification of the TPC-identified protons and antiprotons ($\bar{p}$) can be checked. Table 2.1 shows the probability that the TOF system agrees with the TPC PID at the three lowest beam energies. There is significant contamination of the TPC-identified antiprotons by pions and Kaons as the beam energy is decreased. Since the third and fourth moments products of the multiplicity distributions are very sensitive

$\sqrt{s_{NN}}$ (GeV)	p (%)	K+π (%)	$\bar{\text{p}}$ (%)	K$^-$+π^- (%)
7.7	97.9	1.8	62.1	37.3
11.5	96.6	3.0	74.9	24.3
19.6	96.7	2.8	91.9	7.1

Table 2.1 : The purity of protons and antiprotons identified using the "TPC-only" PID method and 0.4<p$_T$<0.8 GeV cuts at beam energies of 7.7, 11.5, and 19.6 GeV.

to any experimental sources of fluctuations, contamination must be removed. Indeed, it was observed that when TPC-only PID was used, the moments products were suppressed relative to a PID method that required the TOF information. In addition, TPC-only PID with an upper p$_T$ cut and no momentum cut, it was observed that the most central bin (0-5%) of the fourth moments product of net-protons could be further suppressed relative to the other centrality bins. To avoid the potential bias from PID contamination, TOF information was required to be part of the PID method used in this analysis. The use of the TOF information, which extends to higher momentum values than does the TPC PID, also increases the overall measurement efficiency. According to Sec. 1.3, this increases the sensitivity of the present measurements to critical behavior.

Here, a hybrid PID algorithm was used that combined the TPC and TOF detector information. On the left side of Fig. 2.5, individual bands can be seen for identified charged particles. In a specific narrow slice in momentum, the average values of the dE/dx for different particles are distinct. Over many events, the dE/dx distributions have a resolution characterized by a standard deviation, σ. A cut of two standard deviations on either side of the mean was done on the dE/dx information from the TPC. No upper momentum cut is applied at that point. Then, a cut is made on the

mass-squared from the TOF detector, and an upper momentum cut of 1.6 GeV/c for pions and Kaons and 2.8 GeV/c for protons is then applied. A p_T>0.4 GeV/c cut is used for protons to suppress the contamination from "spallation" protons created in the beam pipe. A p_T<2 GeV/c cut is used to decrease the contribution from particles in jets.

2.3   Data sets

RHIC undertook a Beam Energy Scan (BES) in the years 2010 and 2011 in part to understand the phase diagram of the hot and dense nuclear systems created in heavy-ion collisions [12]. By varying the beam energy, nuclear systems freeze out at different points in the phase diagram, as illustrated in Fig. 1.3. The data presented in this thesis was measured by the STAR detector in Au+Au collisions at beam energies, $\sqrt{s_{NN}}$, of 7.7, 11.5, 19.6, 27, 39, 62.4, and 200 GeV.

Year	$\sqrt{s_{NN}}$ (GeV)	Events (M)	$\langle\mu_B\rangle$ (MeV)
2010	7.7	4.9	421
2010	11.5	16.6	316
2011	19.6	27.5	206
2011	27	48.8	156
2010	39	58.4*	112
2010	62.4	59.7*	73
2011	200	46.7*	24

Table 2.2 : The year, beam energy, number of events, and average baryochemical potential, $\langle\mu_B\rangle$, for the data sets used in the present analysis. The $\langle\mu_B\rangle$ values are from the parametrization in Ref. [8]. The event totals marked with an asterisk indicate that only a fraction of the available dataset was analyzed.

Shown in Table 2.2 is a summary of the data sets analyzed here. The first column gives the year the data sample was collected, the second column gives the beam energy, and the third column gives the number of events that were collected. The final column gives the average values of the baryochemical potential, μ_B, calculated using the parametrization described in Ref. [8] (see also Sec. 1.1.2). As the value of the beam energy decreases, the average value of μ_B increases. Varying the beam energy from 200 GeV to 7.7 GeV allows one to explore collisions with μ_B ranging from 24 to 420 MeV, respectively, on average.

Before the data can be analyzed, work needs to be done to calibrate the data for physics analysis. Over the course of about a year, the TOF and TPC detectors undergo numerous calibrations to get the best timing and tracking information possible. The calibrated dataset is organized into so-called "MuDSTs," which contain all of the track and timing information. The MuDSTs are distilled into smaller versions called nanoDSTs containing only the information necessary for this analysis, which were copied to local computers at Rice University for analysis.

2.4 Centrality

As described in Sec. 1.1.1, the multiplicity of tracks measured in the TPC allows the centrality of the collision to be inferred. However, an injudicious choice of the centrality variable used can affect the value of the moments products calculated from the resulting centrality-selected event sample.

Early STAR results [46] for the moments products using the STAR standard centrality definition, called "refmult," showed strong autocorrelations that suppressed the values of the moments products. The moments products values for net-charge, for example, were negative. This mathematical autocorrelation arises from the fact that

the observable (moments of charged particles) used the same particles involved in the centrality definition. The centrality cuts thus sculpted the multiplicity distributions and biased the moments products values.

In order to avoid such autocorrelations in this analysis, the kinematic region where the centrality was defined was chosen to be independent of the analysis region, as depicted in Fig. 2.6. In this figure, the pseudorapidity distributions of charged particles at beam energies of 19.6 and 200 GeV are shown. The centrality was defined using primary tracks with pseudorapidities in the range $0.5<|\eta|<1.0$ (hashed regions in this figure), the total number of which is called "refmult2." The moments analysis was then performed using tracks with pseudorapidities $|\eta|<0.5$ (solid gray regions in this figure).

The refmult2-based centrality definition was further improved by correcting it for the time-dependent luminosity of the beams and for the location of the primary vertex. The improved centrality definition is called "refmult2corr." Fig. 2.7 shows the centrality definition based on refmult2corr at a beam energy of 39 GeV. The Glauber model fit [4] is shown in red, and the data is shown in black. The Glauber model fits the data well for all but the most peripheral collisions. This disagreement at low particle multiplicities is due to known inefficiencies of the STAR event trigger in the most peripheral collisions. The Glauber model describes the data similarly well at all of the presently studied beam energies.

Eight centrality bins, defined using the Glauber simulation of the refmult2corr distributions, were used in this analysis: 0-5% (most central), 5-10%, 10-20%, 20-30%, 40-50%, 50-60%, 60-70%, and 70-80% (most peripheral). The cutoff values of refmult2 for each of these centrality bins for the 39 GeV data can be seen as the vertical lines in Fig. 2.7.
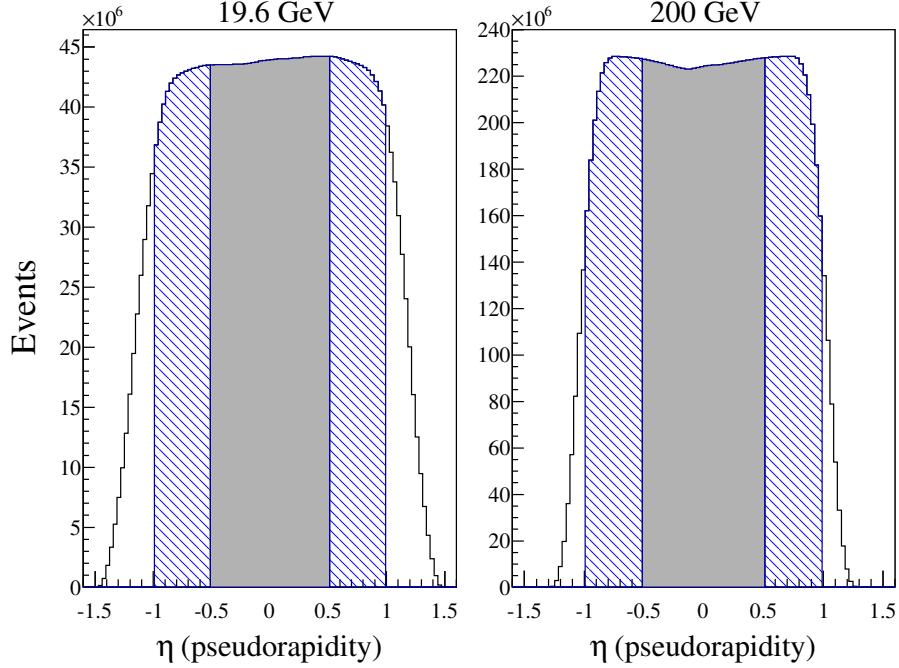
Figure 2.6 : An example histogram of the number of tracks as a function of pseudorapidity at beam energies of 19.6 (left frame) and 200 (right frame) GeV. The hashed region is where the centrality was defined. The solid gray region is where the present moments analysis was performed.

2.5   Good run and event selection

Throughout the present analysis, minimum-bias data sets were used from RHIC runs 10 and 11. A minimum-bias event is one that has occurred in the center of the STAR detector with the minimum amount of additional selectivity on the event. To ensure a nearly uniform detector acceptance, a cut of 30 cm was made on the maximum absolute value of the z-position of the reconstructed primary vertex. The radial position of the primary vertex was required to be less than 1.2 cm to eliminate beam-on-beam-pipe events. The TOF is a fast detector, with hits only being registered from the triggered beam crossing. However, the TPC is much slower, and can contain tracks from other crossings. To suppress this background, it was required that TOF
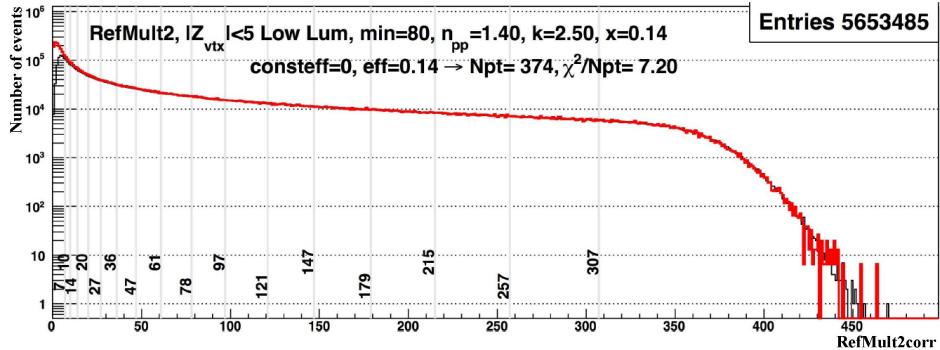
Figure 2.7 : An example of a reference multiplicity histogram (black line) with a Glauber model fit (red line) at 39 GeV. The x-axis is the reference multiplicity refmult2corr.

had at least five hits in the triggered event.

Good run determination

RHIC is "filled" with gold beams many hundreds of times in a several-month-long RHIC run. These fills last between 15 minutes and 8 hours. Each fill is different in terms of the background levels. As the beam energy decreases, the lateral size of the beam increases, which increases the backgrounds and lowers the relative rate of good events. Also, electronics problems develop throughout the run that may affect the operation of the detectors.

These experimental aspects can have dramatic effects on the values of the statistical moments. Thus, it is important to ensure that time-dependent detector-health or beam-related contributions to the analysis are removed. This "quality assurance" (QA) is done by studying the dependence of various event quantities as a function of time within a RHIC run.

In order to identify bad runs, the dependence of thirteen different experimental observables was plotted as a function of the data-run number. A data run is typically

~20 minutes long. The variables used were

- The average number of total pions identified in the 0-5% centrality bin

- The average number of global tracks per event

- The average number of primary tracks per event

- The average value of refmult2

- The average multiplicity for tracks with pseudorapidities of $|\eta|{<}0.5$

- The average value of the difference between the number of global and primary tracks

- The number of events in a data run

- The average number of lit cells in the TOF detector

- The average transverse distance of primary vertex from the beam line

- The average transverse momentum of the primary tracks

- The average azimuthal angle of the tracks in the TPC

- The average number of pions identified by the TOF detector

- The average number of pions identified by the TPC detector.

For each of the seven data sets at a specific beam energy, these quantities were plotted as a function of the data-run number. An example is shown in Fig. 2.8, which is a plot of the mean refmult2 values versus the data-run number at a beam energy of 19.6 GeV. The region delimited by the blue vertical lines is a range of data runs in which

the detector was performing poorly. Single data-run outliers can also be observed, such as around run index 160 on the x-axis.

Each of these distributions is generally flat throughout an entire RHIC run. This allows the calculation of a mean value and standard deviation of each of these quantities over a RHIC run. One can then use the data-run-by-data-run value with respect to these average values and standard deviations to identify bad data runs. In general, a cut of three standard deviations was made to identify an outlier run for a given observable. If a particular data run was flagged as an outlier by three or more of these variables, it was removed from the analysis. In general, bad data runs were flagged as such by more than three variables.
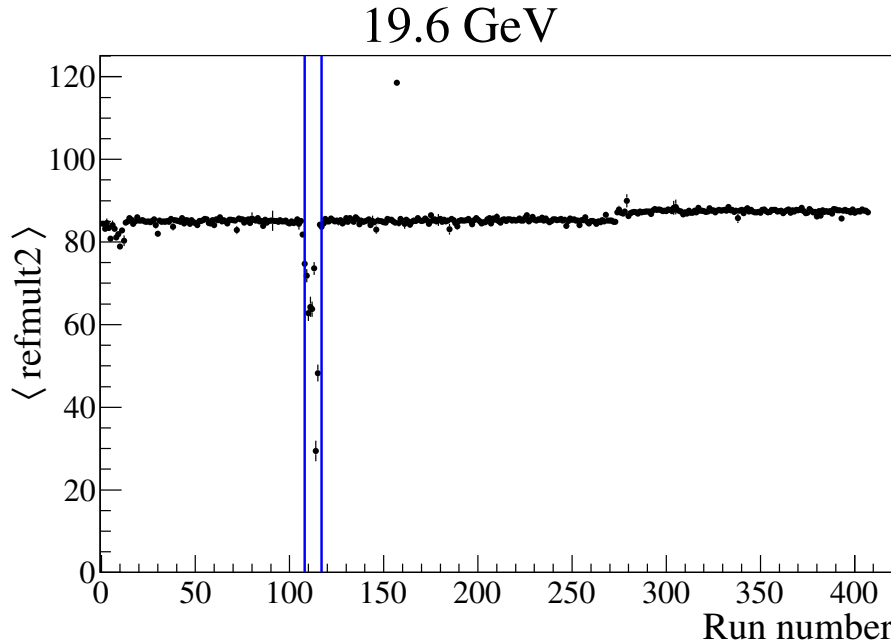
Figure 2.8 : Example QA plot of the mean reference multiplicity, ref-mult2corr, versus the run number at 19.6 GeV.

Bad event removal

At low beam energies, the lateral size of the beam is large. As a result, many of the collisions at low beam energies are from collisions of a gold beam with nuclei in the beam pipe. These events need to removed. In addition, when multiple events occur in the TPC, so-called "pileup" occurs, which produces tracks in the TPC from crossings other than the triggered crossing. The TPC is a slow detector that is open for 50 μs, during which many beam collisions may occur. However, the TOF detector is a fast detector that is open for only 50 ns and sees hits from only the triggered crossing. Thus, besides bad-run rejection, it is also important to reject bad events in good runs.

Shown in Fig. 2.9 is an example of the rejection of bad events. Here, the number of global tracks versus the multiplicity in the TOF detector at a beam energy of 27 GeV is plotted. Pileup can be seen as the events along the y-axis, where the number of global tracks in the TPC far exceeds the number of hits in the TOF detector. One-dimensional "slice" histograms are made for each value of the TOF multiplicity. A mean and standard deviation are calculated for each of these histograms. The events outside of a window that is ± 5 standard deviations from the mean value are rejected, as seen on the right-hand frame of Fig. 2.9. Similar cuts are made in this analysis on other variables versus the TOF multiplicity, such as the number of primary tracks and the value of the refmult2.

2.6   Moments calculation

After performing the good event and track selection, using a non-autocorrelating centrality definition, and correctly identifying charged particles, six different groups
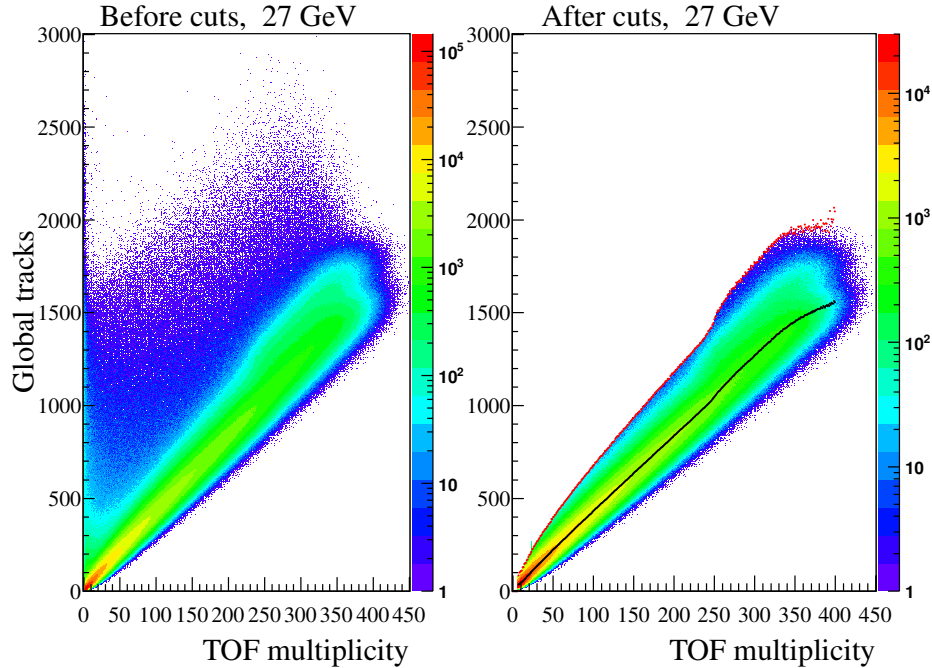
Figure 2.9 : An example event-level QA plot of the number of global tracks versus the multiplicity in the TOF detector at 27 GeV. Shown in the left-hand frame is all of the events. Shown in the right-hand frame is the same data following a 5σ cut to remove the bad events.

of particles are counted in each event: K^+, K^-, p, $\bar{p}$, positively charged particles, and negatively charged particles. The following particle groups are then calculated:

- net-Kaons: the number of positively charged Kaons minus the number of negatively charged Kaons

- net-charge: the number of positively charged particles minus the number of negatively charged particles

- net-protons: the number of protons minus the number of antiprotons

- total-protons: the number of protons plus the number of antiprotons

The multiplicity distributions of each of these particle groups are then stored as a two-dimensional histogram versus refmult2corr. Before the moments can be calculated in different centrality bins, the moments must be averaged so that the moments and moments products values are independent of the width of the centrality bin. The dependence of the moments on the width of the centrality bin is a result of the variations of the impact parameter in the centrality bins [48].

To remove this dependence, the values of the cumulants or moments are calculated for each value of refmult2corr and then averaged within a centrality bin weighted by the number of events in that refmult2corr bin. That is,

$$\sigma = \sum_x w_x \sigma_x \qquad S = \sum_x w_x S_r \qquad K = \sum_x w_x K_x, \qquad (2.8)$$

where x is a value of refmult2corr and w_x is the weight, defined as $w_x = n_x / \sum_x n_x$. Once this correction is performed, the values of the moments and moments products are independent of the width of the centrality bins.

2.7 Uncertainty estimates for the moments

The error bars need to be well understood to ascribe significance to any enhancement potentially resulting from the CP. The STAR collaboration investigated different approaches to calculate the uncertainties of the moments products. Four different uncertainty methods were investigated:

- Analytical - Assumes each moment is uncorrelated and the uncertainty is calculated using the derivatives of the analytic equations. This overestimates the uncertainties because of nonzero covariances between the different moments.

- Subgroup - The data sample is split into four or five subgroups. For each subgroup, the standard deviation of the means of the moments is calculated.

The assigned error is then this standard deviation divided by the square root of the number of subgroups. This method works well if the data samples are large, which is not the case at the lowest beam energies [49].

- Bootstrap - If N is the number of events in the data sample, a randomized data set is formed by selecting N random events from the data sample. Then, the randomized data set is resampled Z times. The standard deviation of the Z resampled groups is the uncertainty [50]. This method is computationally expensive.

- Delta Theorem - Based on the so-called Delta Theorem in statistics that allows the approximation of the distribution of a transformation [51].

The Delta Theorem approach was chosen as the best estimator of the uncertainties of the statistical moments. It is now described.

The deviate is an event-by-event quantity defined using the value, N, and the average value, $\langle N \rangle$, over the whole sample,

$$\delta N = N - \langle N \rangle. \tag{2.9}$$

The central moment, μ_n, of order n is defined using the deviate as

$$\mu_n = \langle (\delta N)^n \rangle = \langle (N - <N>)^n \rangle. \tag{2.10}$$

The normalized central moment of order n, m_n, is the central moment, μ_n, divided by the standard deviation, σ, to the power of n,

$$m_n = \mu_n / \sigma^n = \langle (N - <N>)^n \rangle / \sigma^n. \tag{2.11}$$

The uncertainty expressions for the individual moments from the Delta Theorem are then given by

$$\mathrm{Var}_\sigma = (m_4 - 1)\sigma^2/(4E), \tag{2.12}$$

$$\text{Var}_\text{S} = [9 - 6m_4 + m_3^2(35 + 9m_4)/4 - 3m_3m_5 + m_6]/E, \qquad (2.13)$$

and

$$\text{Var}_\text{K} = [-m_4^2 + 4m_4^3 + 16m_3^2(1 + m_4) - 8m_3m_5 - 4m_4m_6 + m_8]/E, \qquad (2.14)$$

where E is the number of events. The uncertainty expressions for the moments products $S\sigma$ and $K\sigma^2$ are given by

$$\text{Var}_{S\sigma} = \frac{\sigma^2}{E}[9 - 6m_4 + m_3^2(6 + m_4) - 2m_3m_5 + m_6], \qquad (2.15)$$

and,

$$\text{Var}_{K\sigma^2} = \frac{\sigma^4}{E}[-9 + 6m_4^2 + m_4^3 + 8m_3^2(5 + m_4) - 8m_3m_5 + m_4(9 - 2m_6) - 6m_6 + m_8]. \quad (2.16)$$

2.8 Baselines

After the moments products values and uncertainties are calculated, their values must be compared to appropriate baselines in order to look for the possible beam-energy-localized enhancements that could be indicative of a critical point. Five such baselines are

- Poisson statistics - This assumes each parent multiplicity distribution (positive and negative particles) is a Poisson distribution. When two independent Poisson distributions are subtracted (e.g., net moments), the resulting distribution is a Skellam distribution. The moments products are then calculable using the means (M) of each Poisson distribution as

$$(S\sigma)^{\text{Poisson}} = (M^+ - M^-)/(M^+ + M^-) \qquad (2.17)$$

$$(K\sigma^2)^{\text{Poisson}} = 1, \qquad (2.18)$$

where M^+ (M^-) is the average value of the multiplicity of positively (negatively) charged particles. If the two Poisson distributions are instead added (e.g., total moments), the Poisson expectation for both $S\sigma$ and $K\sigma^2$ is unity. The Poisson expectation will be shown as blue lines in the results shown in the next chapter.

- (Negative) Binomial - The Poisson distribution is the limiting form of a (negative) binomial [(N)BD] in the case that the mean and variance are strictly equal. The means and variances in the present data are similar, but not equal, in general. If the mean is larger than the variance, a Binomial Distribution (BD) baseline is used. If the mean is smaller than the variance, a Negative Binomial Distribution (NBD) is used. If the mean is equal to the variance, a Poisson Distribution is used. The BD baseline for the moments products $S\sigma$ and $K\sigma^2$ uses the parameter p, defined as p=1-σ^2/μ, where μ is the mean and σ^2 is the variance. Then, the BD baseline for $S\sigma$ is given by

$$(S\sigma)^{\mathrm{BD}} = 1 - 2p \ (\mu > \sigma^2), \tag{2.19}$$

and the BD calculation of the moments product $K\sigma^2$ is

$$(K\sigma^2)^{\mathrm{BD}} = 1 - 6p + 6p^2 \ (\mu > \sigma^2). \tag{2.20}$$

For the NBD baselines of the moments products $S\sigma$ and $K\sigma^2$ the parameter p is defined as p=μ/σ^2. Then, the NBD baseline for $S\sigma$ is given by

$$(S\sigma)^{\mathrm{NBD}} = (2 - p)/p \ (\mu < \sigma^2), \tag{2.21}$$

and the NBD calculation of the moments product $K\sigma^2$ is

$$(K\sigma^2)^{\mathrm{NBD}} = (6 - 6p + p^2)/p^2 \ (\mu < \sigma^2). \tag{2.22}$$

The (N)BD expectation will be shown as magenta lines in the next chapter.

- Hadron Resonance Gas (HRG) [52, 53] - This is a thermal model that assumes no critical phenomena. The moments products are functions of thermodynamic parameters (T and μ_Q) and the electric charge (Q_i) of the particles. The particle multiplicity distributions are assumed to be independent Poisson distributions, and thus are consistent with the Poisson expectation if only particles with electric charge of one, such as pions, Kaons, and protons, are considered. However, in the case of net-charge, baryons with an electric charge of two, such as Δ resonances, also contribute. The HRG expectation for the moments products of net-charge is:

$$(S\sigma)^{\mathrm{HRG}} = \tanh(Q_i \mu_Q / T) \tag{2.23}$$

and

$$(K\sigma^2)^{\mathrm{HRG}} \sim 1.8 \tag{2.24}$$

where the value of $(K\sigma^2)^{\mathrm{HRG}}$ is weakly dependent on the beam energy. The $S\sigma^{\mathrm{HRG}}$ values for net-charge are calculated in Ref. [52] using the thermodynamic parameters in Ref. [53]. The HRG expectation will be shown as red lines in the next chapter.

- Mixed events - "Mixed" events are created by randomly selecting a number of particles with positive charge and a number of particles with negative charge at a given value of refmult2corr from the experimentally measured parent distributions for each particle. These numbers are subtracted (added) to form a net-particle (total-particle) value randomly over the same number of events as in the experimental data [54]. Then, the same moments analysis can be

performed. This mixed-event data set has the same number of events as the original data set, but all intra-event correlations between the numbers of positively and negatively charged particles are removed. The mixed-event values will be shown as green lines in the next chapter.

- Central Limit Theorem - The multiplicity distribution at any value of the centrality is assumed to result from many independent source distributions [46]. The number of sources is assumed to scale with the centrality, i.e., the $\langle N_{part} \rangle$ calculated from the Glauber model [4]. The individual moments for a centrality bin, i, are then

$$M_i = M_x \cdot C \cdot N_{part}, \tag{2.25}$$

$$\sigma_i^2 = \sigma_x^2 \cdot C \cdot N_{part}, \tag{2.26}$$

$$S_i = S_x / \sqrt{C \cdot N_{part}}, \tag{2.27}$$

and

$$K_i = K_x / (C \cdot N_{part}), \tag{2.28}$$

where C is a constant and $_x$ denotes the sum of the moments values at all centralities. Using only these parameters, the CLT predicts the centrality dependence of the second, third, and fourth statistical moments.

Chapter 3

Results

Since the moments products are related to the susceptibilities of conserved quantities, the results for the moments products of net-Kaons (a proxy of strangeness), net-charge, and net-protons (a proxy of baryon number) are of interest. In addition, if the critical point manifests itself as a divergence of the correlation length, a phenomenological model predicts that total moments, especially of protons, may be more sensitive to it, so the results for total-protons are also of interest. The experimental results of the moments products for these particle groups are described in this chapter. The signal of a critical point is expected to be a beam-energy and centrality localized enhancement of the moments products resulting from the system, on average, freezing out near the critical point. The error bars shown are only statistical and are calculated using the Delta Theorem [51].

3.1   Centrality dependence of the moments and CLT

Shown in Fig. 3.1 is the centrality dependence of the mean (M), standard deviation (σ), skewness (S), and kurtosis (K) of the net-proton multiplicity distributions in Au+Au collisions at $\sqrt{s_{NN}}$ = 7.7, 11.5, 19.6, 27, 39, 62.4, and 200 GeV. The mean and standard deviation increase monotonically as a function of $\langle N_{part} \rangle$. The skewness and kurtosis decrease monotonically as a function of $\langle N_{part} \rangle$.

The expectations from the CLT (Sec. 2.8) are shown as the dashed lines. In

general, the CLT expectations describe the basic trends of the centrality dependence
of the moments of the net-proton and net-charge multiplicities. The fit constant C
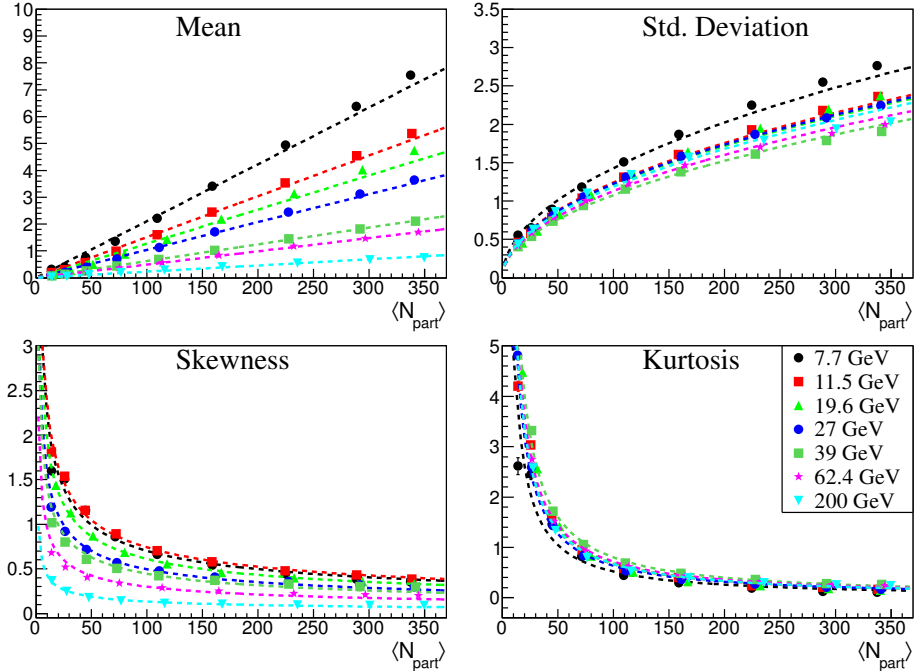
Figure 3.1 : The centrality dependence of the lower four moments (M, σ, S, and K) of the net-proton multiplicity distributions versus the average number of participant nucleons at 7.7, 11.5, 19.6, 27, 39, 62.4, and 200 GeV. The dashed lines show the expectations from the Central Limit Theorem.

from Eqs. 2.25-2.28 for each beam energy is listed in Table 3.1. For net-charge, the
values of C agree across the different beam energies to within $\sim$5%, with the exception
of the date at 200 GeV. The values of C also agree across the different beam energies
to within $\sim$5% for net-protons, with the exception of the data at 200 GeV. The fit
constant values are in generally good agreement between net-protons and net-charge.

To better see the difference between the CLT expectation and the data, "residual"
plots were made of the difference between the dashed curves and the data points in
Fig. 3.1. An example plot of the kurtosis residual is shown in Fig. 3.2, with the

$\sqrt{s_{NN}}$ (GeV)	C ($\times 10^{-4}$) net-charge	C ($\times 10^{-4}$) net-proton
7.7	8.2	8.0
11.5	8.2	8.0
19.6	8.0	7.8
27	8.1	7.9
39	8.0	7.8
62.4	7.9	7.7
200	7.4	7.2

Table 3.1 : The fit constant, C, of the CLT fits as a function of beam energy for net-charge and net-protons.

different energies shown in the different frames. Red lines are drawn at zero for reference. Even though the CLT expectation appears to reasonably describe the data in Fig. 3.1, the residuals show that there are systematic deviations for the kurtosis, especially in peripheral collisions. Such trends were also seen in the residual plots for other moments, and for the other particle groups of net-charge and net-protons (not shown). For both particle groups, the mean and the standard deviation residuals approach zero as the collisions become more central. The skewness and kurtosis values agree to ~10-20% with the CLT expectations, with the largest disagreement occurring in the most peripheral centrality bins. Thus, while the CLT appears in Fig. 3.1 to accurately describe the data, the residuals indicate that it is accurate only to ~20% and that there are systematic deviations versus the beam energy and centrality.
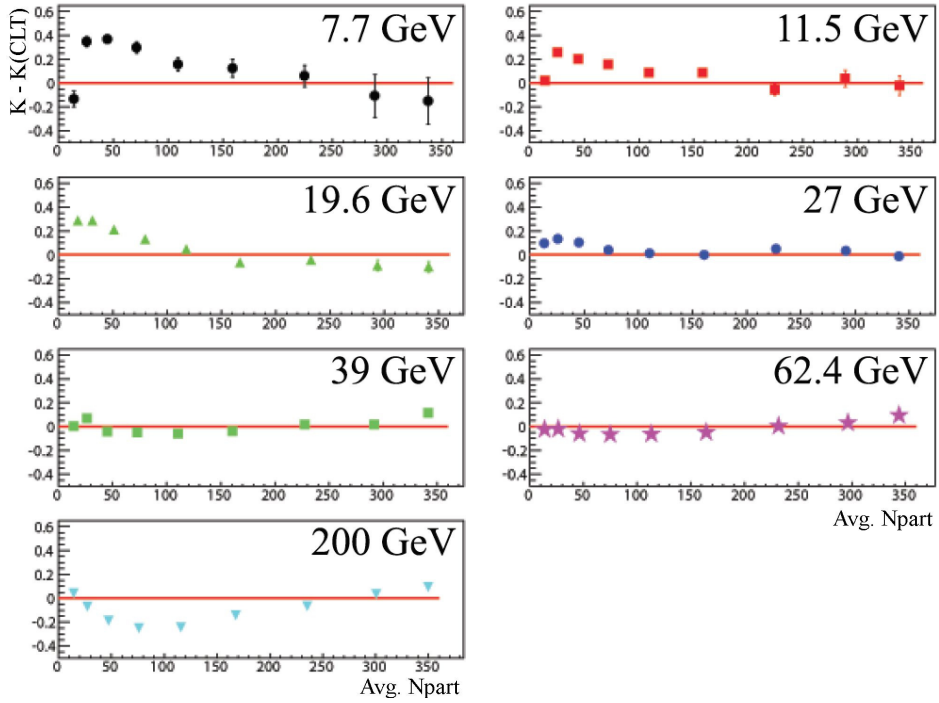
Figure 3.2 : A residual plot showing the CLT expectation subtracted from the value of the kurtosis of the net-proton multiplicity distribution versus the average number of participant nucleons. Different energies are shown in different frames, with 7.7 GeV in the upper left and 200 GeV at the bottom. Red lines are drawn at zero for reference.

3.2 Centrality dependence of the moments products

The centrality dependence of the moments products $S\sigma$ and $K\sigma^2$ for four particle groups (net-Kaons, net-charge, net-protons, and total-protons) will now be shown. The experimental values will be plotted versus the average number of participant nucleons, $\langle N_{part} \rangle$, obtained from the Glauber calculations. The most central (peripheral) collisions have the largest (smallest) values of $\langle N_{part} \rangle$. These will be compared to the baselines described in Sec. 2.8.

3.2.1   Net-Kaons

Shown in Fig. 3.3 and Fig. 3.4 is the centrality dependence of $S\sigma$ and $K\sigma^2$, respectively, for net-Kaons at seven different beam energies ranging from 7.7-200 GeV. The moments products $S\sigma$ and $K\sigma^2$ are generally independent of the centrality to $\sim 15\%$. For $S\sigma$, the values from the data decrease as the beam energy increases. Shown in blue are the Poisson baselines. The measured values are above the Poisson baseline at all beam energies. Shown as the magenta lines are the (N)BD expectations. The mixed-events values are shown as the green lines. The mixed-events values and the (N)BD expectations describe the data much better than the Poisson baseline for both moments products. This good agreement between the (N)BD expectations and the data indicates that intra-event correlations do not have a significant contribution to the moments products values for net-Kaons.

3.2.2   Net-charge

Shown in Fig. 3.5 and Fig. 3.6 is the centrality dependence of $S\sigma$ and $K\sigma^2$, respectively, of net-charge for the seven different beam energies ranging from 7.7-200 GeV. Shown as blue lines are the Poisson expectations. The moments products $S\sigma$ and $K\sigma^2$ are generally independent of centrality and above the Poisson expectation at all beam energies. Shown as the magenta lines are the (N)BD expectations. The (N)BD baseline describes the $S\sigma$ data very well. The (N)BD baseline is above the $K\sigma^2$ data in peripheral collisions but approaches the data values in central collisions. A similar trend was also seen in simulations [55]. The mixed-events values are shown as the green lines. The $S\sigma$ data is well described by the mixed-event approach for beam energies below 62.4 GeV. In the most-central bins at 62.4 and 200 GeV, the mixed-event values grow increasingly negative (out of the range of the plot). Simi-
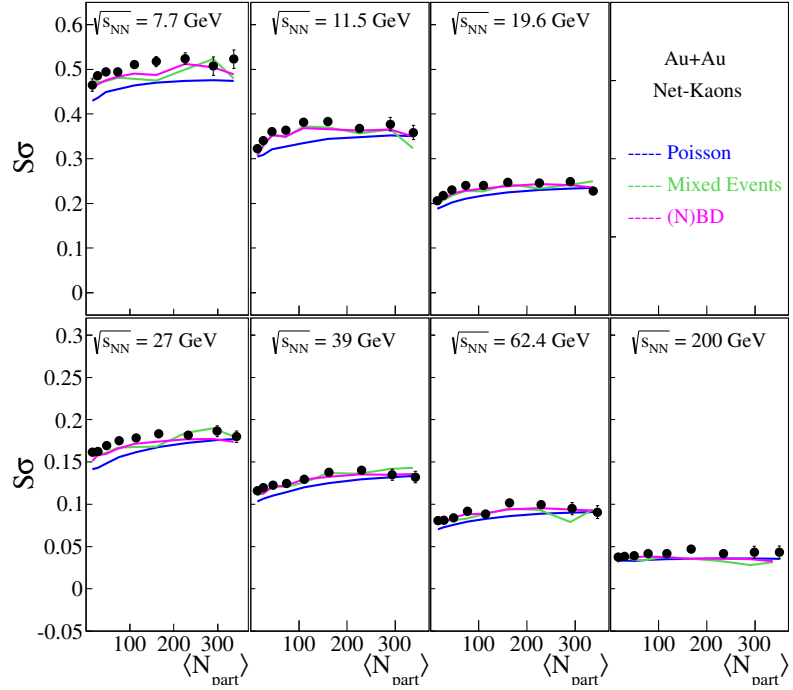
Figure 3.3 : The centrality dependence of Sσ of net-Kaons at beam energies from 7.7-200 GeV. The baselines are shown as the colored lines.
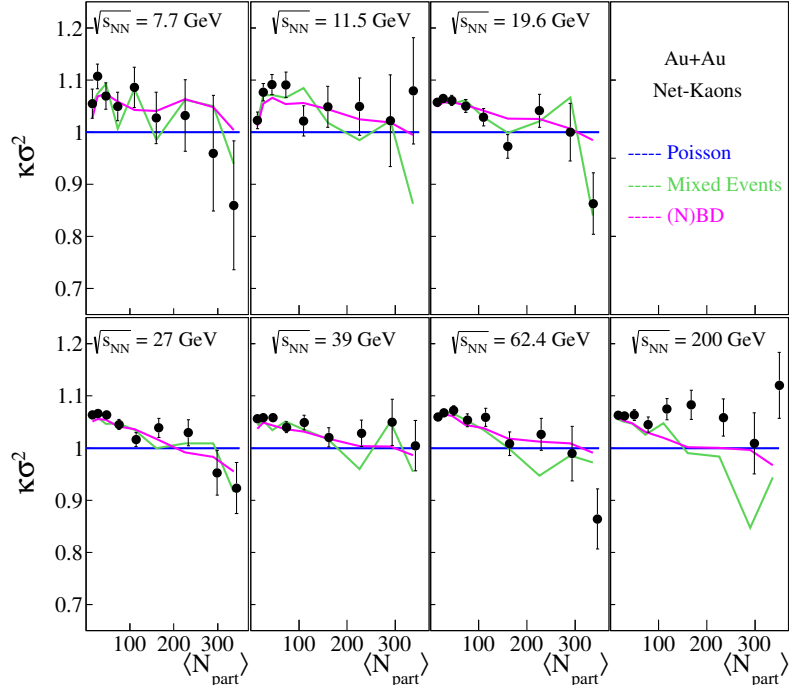
Figure 3.4 : The centrality dependence of Kσ² of net-Kaons at at beam energies from 7.7-200 GeV. The baselines are shown as the colored lines.
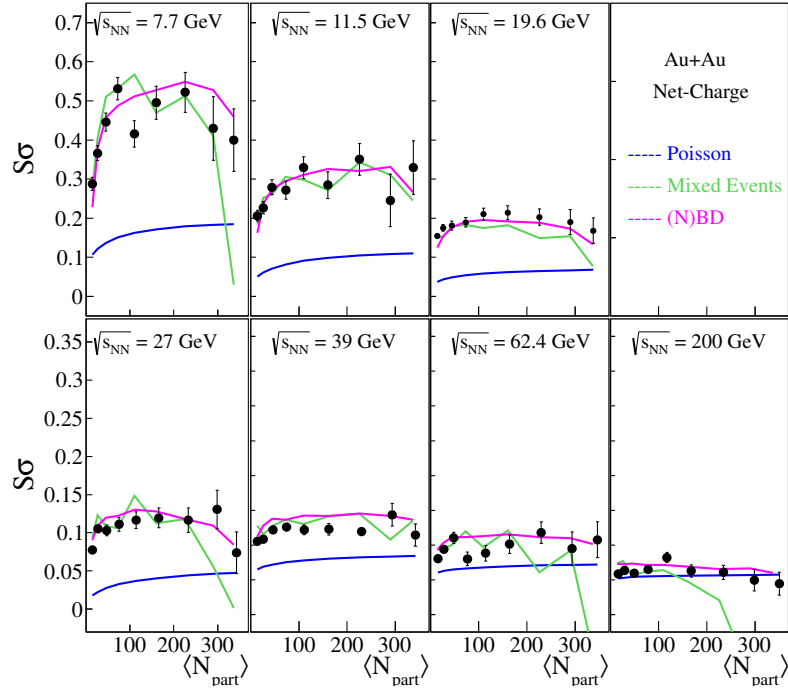
Figure 3.5 : The centrality dependence of Sσ of net-charge at beam energies from 7.7-200 GeV. The baselines are shown as the colored lines.
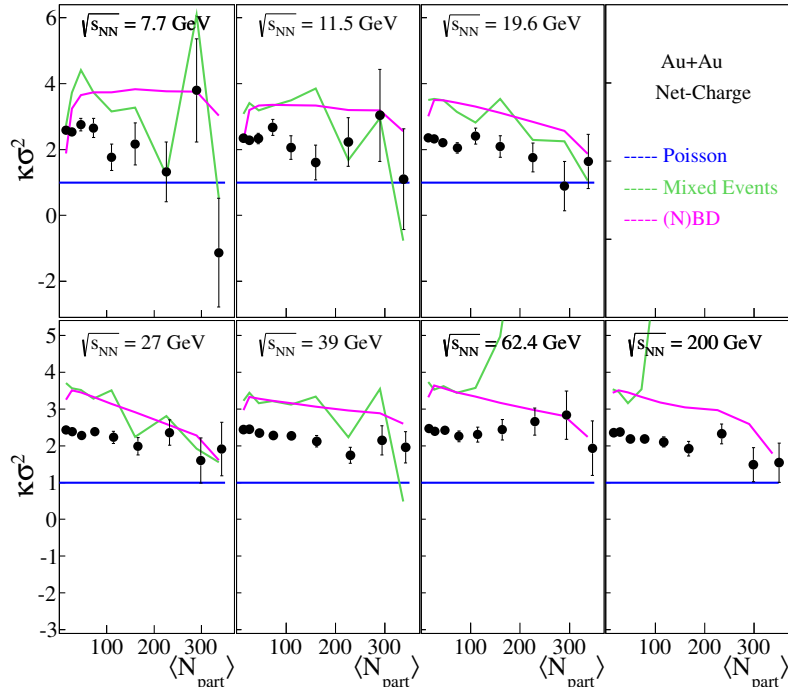

Figure 3.6 : The centrality dependence of Kσ^2 of net-charge at beam energies from 7.7-200 GeV. The baselines are shown as the colored lines.

larly, the $K\sigma^2$ mixed-event values become increasing positive at 62.4 and 200 GeV in central collisions (out of the range of the plot). The strong discrepancies between the values of the moments products and those from the mixed-events are indicative of the importance of intra-event correlations from electric charge conservation laws.
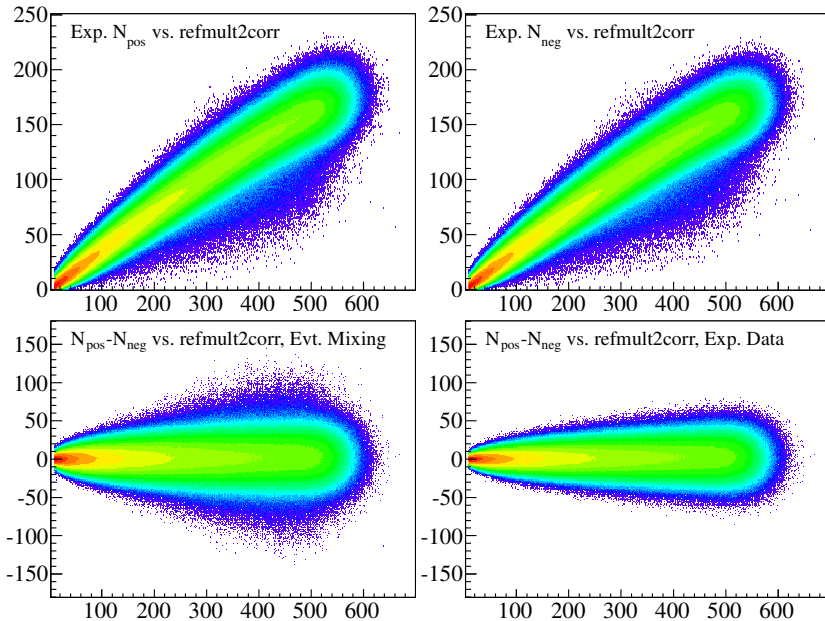
Figure 3.7 : The number of positively charged particles and the number of negatively charged particles at 200 GeV versus refmult2corr (upper left and upper right, respectively) and the net-charge distribution from event mixing and the experimental data (lower left and lower right frames, respectively). Figure from [56].

The importance of intra-event correlations is illustrated in Fig. 3.7. Shown in the upper two frames are the experimental values of the number of positively charged particles (N_{pos}) and the number of negatively charged particles (N_{neg}) versus refmult2corr at 200 GeV, respectively. The values from these distributions are sampled in the mixed-event approach to form the net-charge versus refmult2corr distribution shown in the lower-left frame. The moments products from the data shown in this

frame are the green lines in Figs. 3.5-3.6. The experimental distribution of N_{pos}-N_{neg} versus refmult2corr is shown in the lower-right frame of Fig. 3.7. This distribution is clearly much narrower than the distribution obtained using the mixed-events approach. In both upper frames, an excess, or tail, below the diagonal is observed (e.g. N_{pos} or N_{neg} of ~50 at refmult2corr of ~400). The mixed-event approach samples from each distribution independently, including events in these low tails. The resulting N_{pos}-N_{neg} distribution from the event mixing (lower-left of Fig. 3.7) is much wider than the experimental one because in the data the events in the low N_{pos} tail are also in the low N_{neg} tail. The mixed-events approach destroys such intra-event correlations and thus completely fails to describe the net-charge moments products.

3.2.3 Net-protons

Shown in Fig. 3.8 and Fig. 3.9 is the centrality dependence of $S\sigma$ and $K\sigma^2$, respectively, of net-protons at the seven different beam energies. In general, the values of $K\sigma^2$ for net-protons decreases as the collisions become more central. Shown as the blue lines are the Poisson expectations. The moments product $S\sigma$ shows a significant deviation from the Poisson expectation at beam energies below 39 GeV. The data for the most central collisions lie below the Poisson expectation at 11.5, 19.6, 27, and 39 GeV. The values of $K\sigma^2$ are below the Poisson expectation at all centralities for beam energies larger than 11.5 GeV. Shown as the magenta lines are the (N)BD expectations. With the exception of the $K\sigma^2$ values at 7.7 GeV, the (N)BD expectations describe the data very well for both moments products. Shown as the green lines are the values from the mixed events. The data follows the mixed-events values for both moments products at all centralities and beam energies. Therefore, the intra-event correlations, such as those from baryon number conservation, have no significant effect on the moments
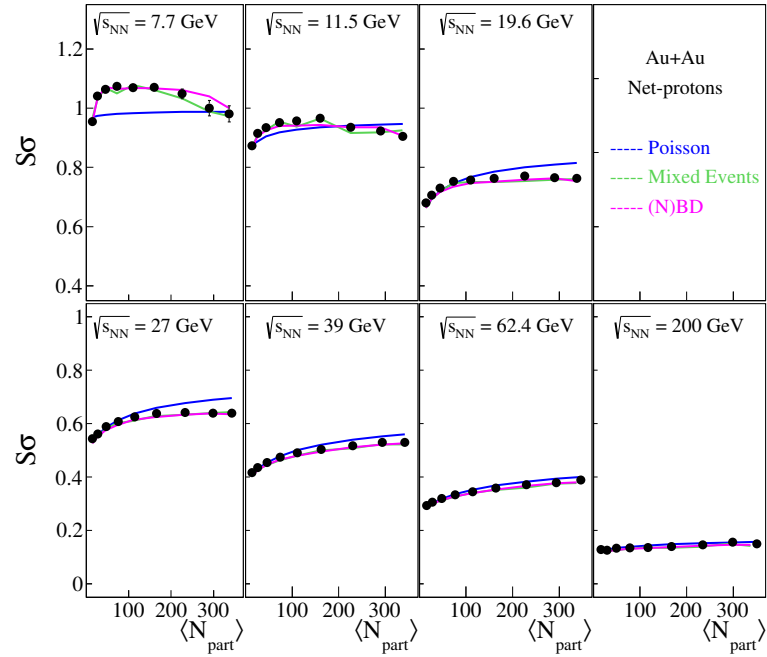
Figure 3.8 : The centrality dependence of Sσ of net-protons at beam energies from 7.7-200 GeV. The baselines are shown as the colored lines.
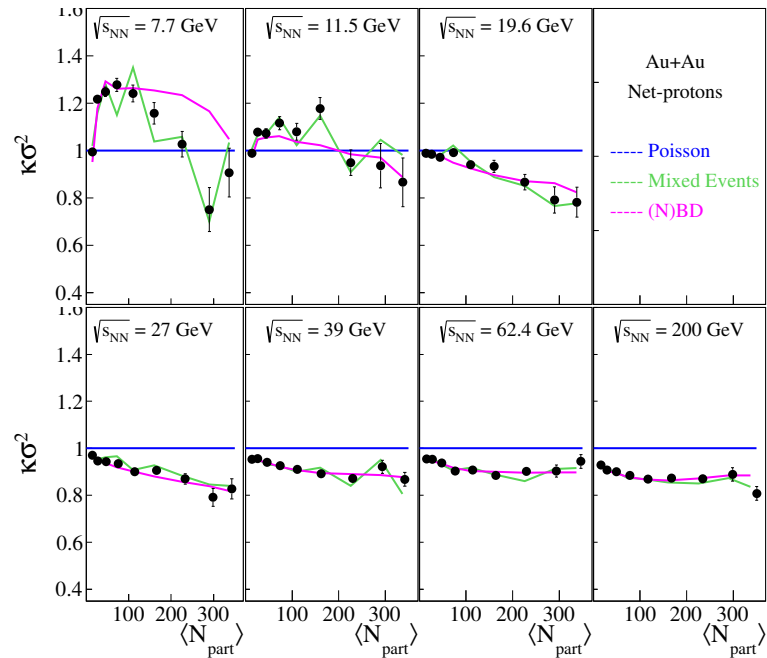
Figure 3.9 : The centrality dependence of Kσ^2 of net-protons at beam energies from 7.7-200 GeV. The baselines are shown as the colored lines.
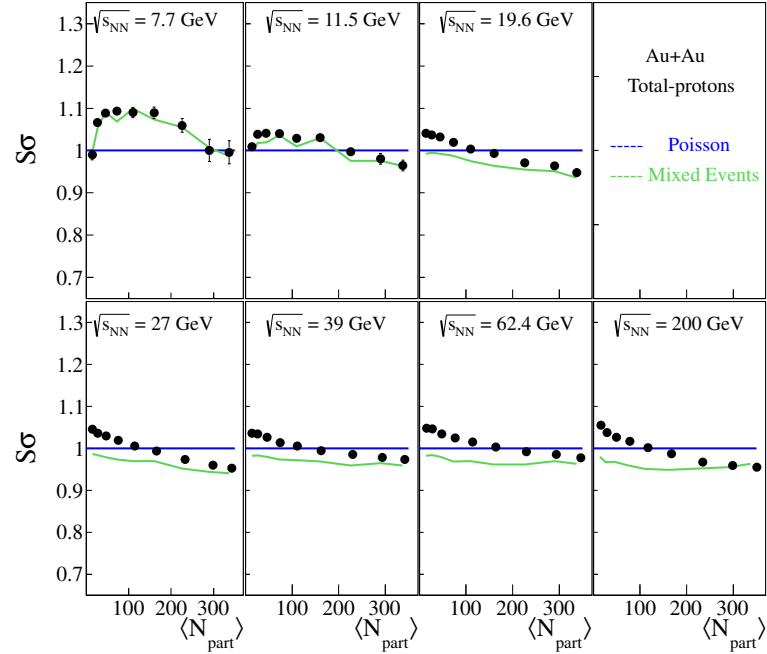
Figure 3.10 : The centrality dependence of Sσ of total-protons at beam energies from 7.7-200 GeV. The baselines are shown as the colored lines.
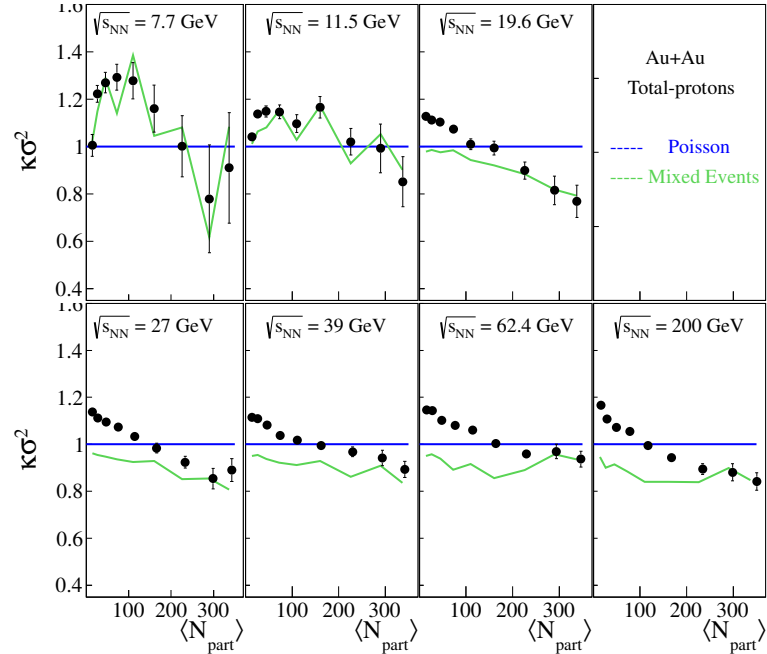

Figure 3.11 : The centrality dependence of Kσ^2 of total-protons at beam energies from 7.7-200 GeV. The baselines are shown as the colored lines.

products for net-protons.

3.2.4 Total-protons

Shown in Fig. 3.10 and Fig. 3.11 is the centrality dependence of $S\sigma$ and $K\sigma^2$, respectively, of total-protons at the seven different beam energies. Both moments products monotonically decrease as a function of increasing centrality. Shown as the blue lines are the Poisson expectations. The Poisson expectation for both of these moments products is unity because the addition of two independent Poisson distributions is also a Poisson distribution (see Sec. 2.8). The moments products $S\sigma$ and $K\sigma^2$ show the same trend at all energies: the values are above the Poisson expectation in peripheral collisions and below the Poisson expectation in central collisions, in general crossing the Poisson expectation at $\sim 30\%$ centrality. Shown as the green lines are the values from the mixed-events method. The mixed events describe the data very well for both moments products at beam energies of 7.7 and 11.5 GeV. At larger values of the beam energy, the data matches the values from the mixed events in the most central collisions but becomes progressively larger than those from the mixed events in more peripheral collisions. This indicates the increasing importance of intra-event correlations for total protons as the collisions become more peripheral. For both $S\sigma$ and $K\sigma^2$, the values from the mixed events at beam energies larger than 11.5 GeV are always below the Poisson expectation.

3.3 Beam-energy dependence of the moments products at 0-5% centrality

The hottest and densest nuclear systems at a given beam energy are created in the most central collisions. If different beam energies produce nuclear systems in dif-

ferent regions of the phase diagram and a tight centrality window tightly constrains the values of the baryochemical potential, critical behavior may manifest itself as a beam-energy localized enhancement of the moments products. The beam-energy dependence of the moments products for the most central five percent of the collisions will be shown for four different particle groups in this section.

Shown in Fig. 3.12 are the values of $K\sigma^2$ (upper frame) and $S\sigma$ (lower frame) for net-Kaons in the 0-5% central collisions. The Poisson baselines are shown as the blue lines, the (N)BD baselines are shown as the magenta lines, and the mixed-events values are shown as the green lines. In general, all the baselines reasonably describe the moments products values. No significant and $\sqrt{s_{NN}}$-localized enhancements are observed.

Shown in Fig. 3.13 are the values of $K\sigma^2$ (upper frame) and $S\sigma$ (lower frame) for net-charge in the 0-5% central collisions. Again, the Poisson baselines are shown as the blue lines, the values from the Hadron Resonance Gas (HRG) model are shown as the red lines, and the (N)BD expectations are shown as the magenta lines. The values of $S\sigma$ are greater than the Poisson expectation, are less than the HRG expectation, but are very well described by the (N)BD expectation in central collisions. The mixed-events values are shown as the green lines. For both moments products, the mixed-events values extends out of the range of the plot (see Sec. 3.2.2). No significant and $\sqrt{s_{NN}}$-localized enhancement of either moments product is observed.

Shown in Fig. 3.14 and Fig. 3.15 are the values of $K\sigma^2$ (upper frame) and $S\sigma$ (lower frame) in the 0-5% central collisions of net-protons and total-protons, respectively. The Poisson baselines are shown as the blue lines, the (N)BD baselines are shown as the magenta lines, and the values from mixed events are shown as the green lines. In general, the moments products of net-protons and total-protons are below the
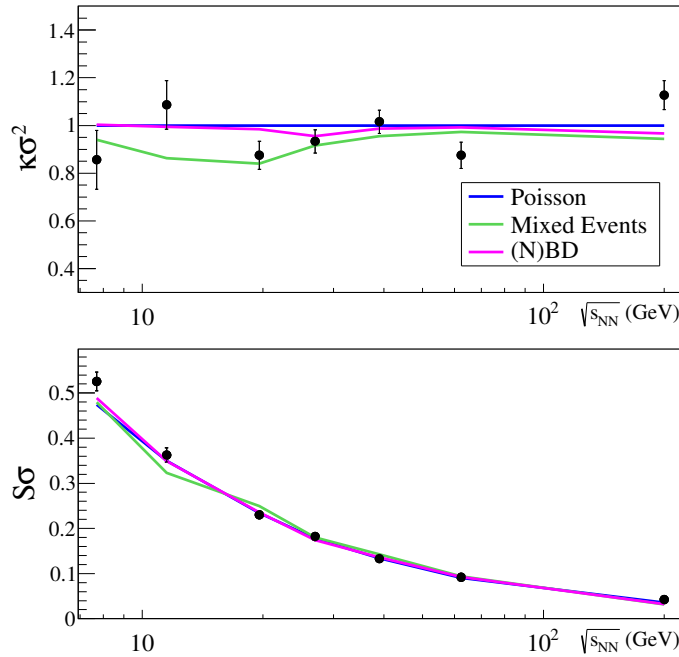
Figure 3.12 : The moments products Sσ and Kσ^2 for net-Kaons for 0-5% central collisions, with the baselines shown as the solid lines.
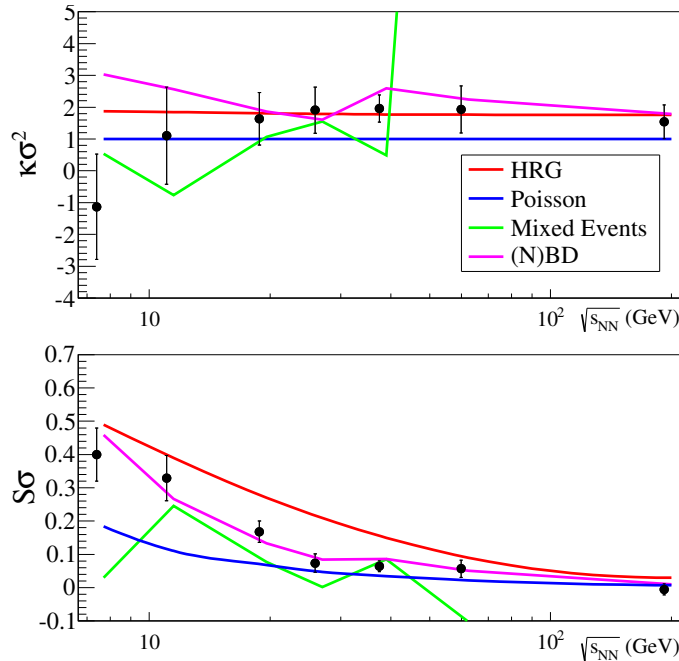
Figure 3.13 : The moments products Sσ and Kσ^2 for net-charge for 0-5% central collisions, with the baselines shown as the solid lines.
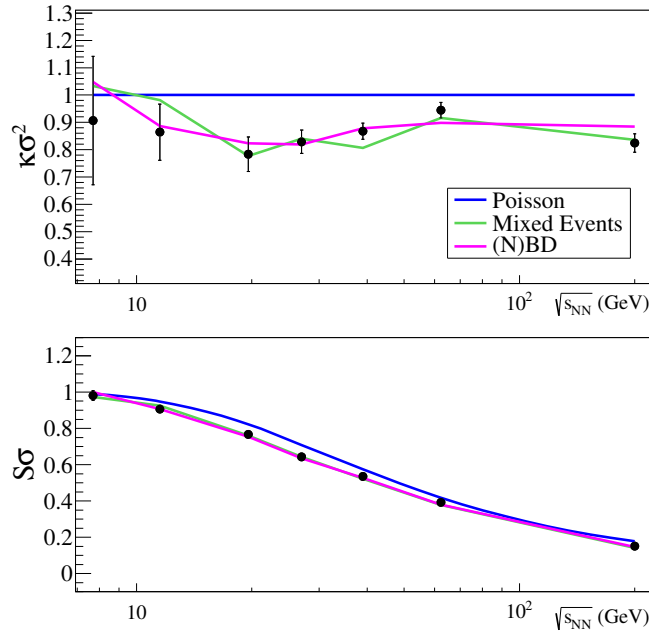
Figure 3.14 : The moments products Sσ and Kσ^2 for net-protons for 0-5% central collisions. The baselines are shown as the colored lines.
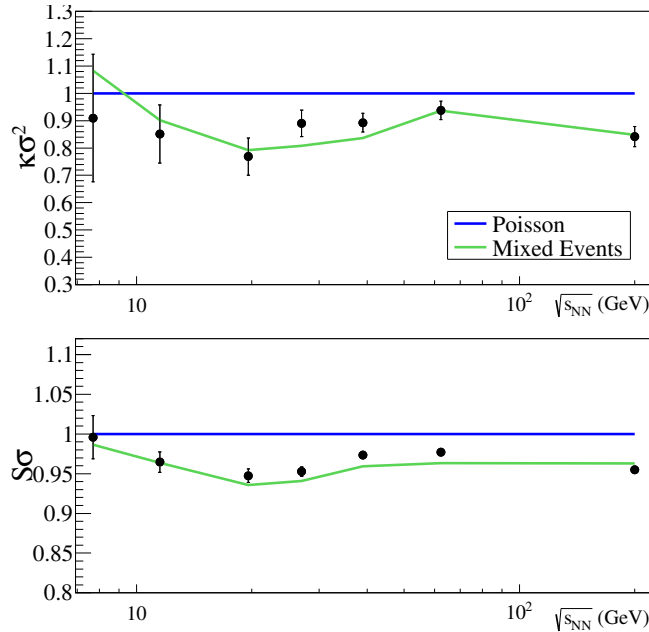

Figure 3.15 : The moments products Sσ and Kσ^2 for total-protons for 0-5% central collisions. The baselines are shown as the colored lines.

Poisson expectations. The data have a weak minimum at a beam energy of 19.6 GeV. This minimum might be seen as the negative contribution to the kurtosis discussed in Sec. 1.2.3, and hence indicative of the proximity of the CP. However, these data points are very well described by the (N)BD and the mixed-events approaches, implying that critical behavior is not responsible for this weak minimum.

3.4 Gating on the event-by-event antiproton-to-proton ratio

In previous sections, it was assumed that using narrow (5% wide) centrality windows tightly constrained the values of μ_B in those samples of events. In other words, it was assumed that the variance of μ_B in a tightly centrality-selected sample of events was small. This may not be a valid assumption [56]. This is shown in Fig. 3.16, where the distribution of baryochemical potential values is plotted for seven different beam energies and two different centrality ranges. These values were obtained by using the statistical hadronization model, THERMUS [5], event-by-event, extracting (μ_B, T) from each event [56]. The different beam energies are given by different colors, with black representing 7.7 GeV and light blue representing 200 GeV. Even in the "narrow" (5% wide) centrality windows, the distributions of μ_B event by event overlap and are rather wide.

To more tightly constrain the events in the phase diagram, one can cut on additional information in each event. The ratio of $\bar{p}/p$ is directly related to the baryochemical potential:

$$\frac{\bar{p}}{p} = e^{-2\mu_B/T}.$$ (3.1)

It has been shown that in these data [9], the average temperature is a very weak function of the centrality and beam energy in central collisions. Thus, the event-by-event ratio of $\bar{p}/p$ is directly related to the apparent value of μ_B event-by-event. The
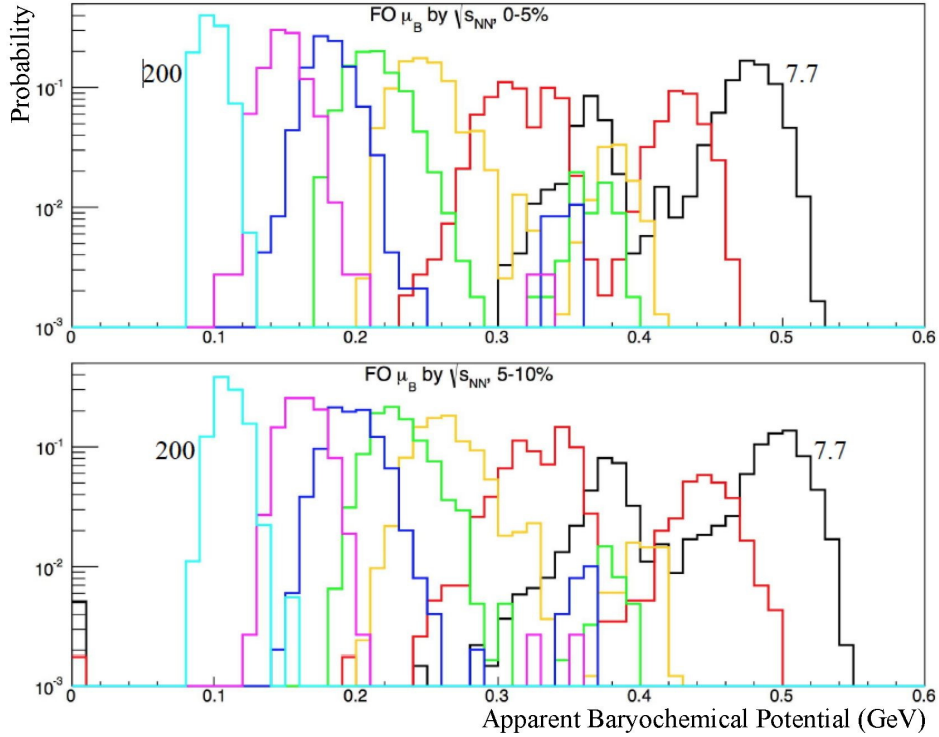
Figure 3.16 : Normalized histograms of the value of the baryochemical potential at freezeout at seven different beam energies (different colors) and two different centrality ranges (0-5% in the upper frame, 5-10% in the lower frame). Figure from Ref. [56]

distribution of the ratio of $\bar{p}/p$ over all beam energies was divided into logarithmically equal width bins, each spanning a range of apparent μ_B of ~ 27 MeV (as shown in Table 3.2). Then, the $K\sigma^2$ values of the proton and kaon moments were analyzed independently in each of the $\bar{p}/p$ bins.

Fig. 3.17 and Fig. 3.18 show the moments product $K\sigma^2$ for net-protons and total-protons, respectively, as a function of the apparent-μ_B bin number for 0-10% centrality. Shown as the green histogram is the mixed-events approach.

Both the net-proton and total-proton $K\sigma^2$ values show a peak around bin number 5 (apparent μ_B values from 142 to 170 MeV) in central collisions. Such an enhancement

Bin	p̄/p ratio	μ_B (GeV)
1	0.020-0.029	0.279-0.252
2	0.029-0.043	0.252-0.225
3	0.043-0.063	0.225-0.197
4	0.063-0.093	0.197-0.170
5	0.093-0.136	0.170-0.142
6	0.136-0.200	0.142-0.115
7	0.200-0.294	0.115-0.088
8	0.294-0.431	0.088-0.060
9	0.431-0.632	0.060-0.033
10	0.632-0.928	0.033-0.005
11	0.928-1.363	0.005-$^-$0.022

Table 3.2 : The antiproton to proton ratio and the corresponding apparent baryochemical potential for each range of the ratio values.

of the moments products values in this apparent μ_B bin is exactly the expected signal for the critical point (see Sec.1.2.3). The values from the mixed events approach reproduce the trend of the data. However, there are still some excesses in the data in bin 5. Since the agreement between the data and the mixed-events approach is excellent for the other bins, further study of any excess is needed.

Fig. 3.19 shows the moments product $K\sigma^2$ for net-Kaons as a function of the apparent-μ_B bin number for 0-10% centrality. Shown are the Poisson (blue) and mixed-event (green) baselines. The Poisson expectation reasonably describes the data across all apparent-μ_B bins for beam energies above 11.5 GeV. The mixed-event approach describes the data well at all energies and apparent-μ_B bins. No peaks are
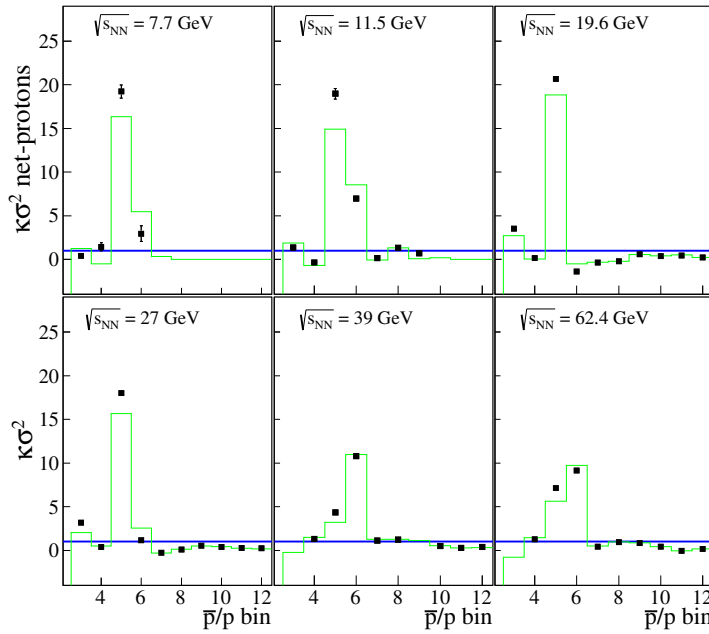
Figure 3.17 : The moments product $K\sigma^2$ for net-protons as a function of apparent-μ_B bin number for 0-10% centrality. The values from the mixed-event approach are shown as the green histogram.
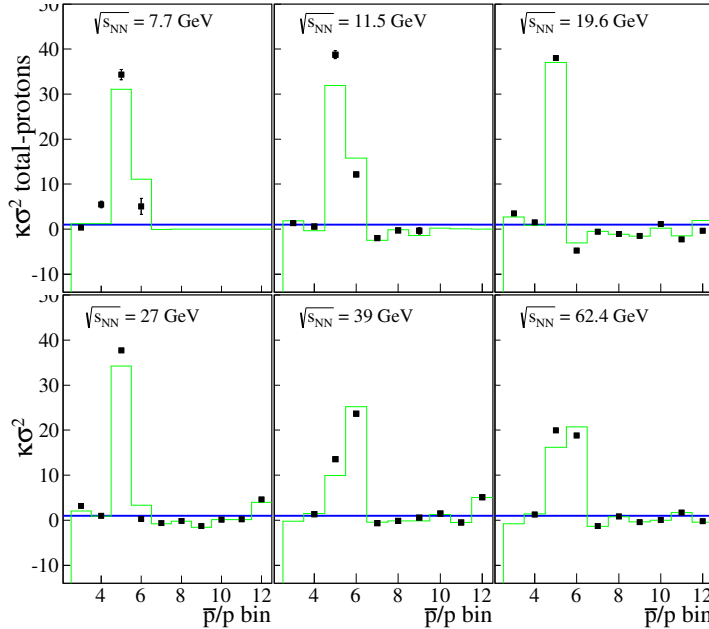
Figure 3.18 : The moments product $K\sigma^2$ for total-protons as a function of apparent-μ_B bin number for 0-10% centrality. The values from the mixed-event approach are shown the green histogram.
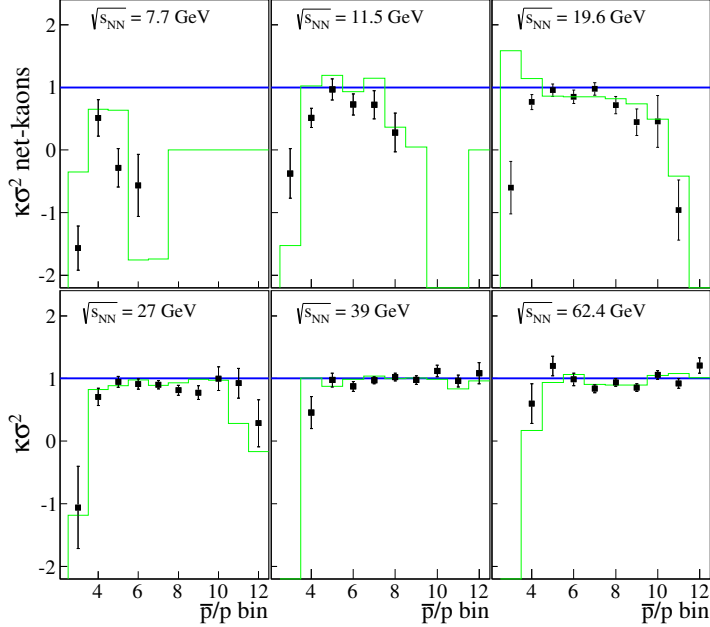
Figure 3.19 : The moments product $K\sigma^2$ for net-Kaons as a function of apparent-μ_B bin number for 0-10% centrality. The values from the mixed-event approach are shown as the green histogram. The simple Poisson expectation is shown as the blue lines.

seen for $K\sigma^2$ of net-Kaons as a function of apparent μ_B values.

3.5   Future directions

At the presently available beam energies, no large beam-energy or centrality-localized enhancement of the moments products is observed for any of the particle groups investigated. However, according to Table 2.2, there are still two large ($\sim$100 MeV wide) gaps in the average values of the baryochemical potential between the presently available data sets. Figure 3.20 shows the same data as Fig. 3.13, except the x-axis is now the average baryochemical potential. The average baryochemical potential is anticorrelated to the beam energy, so 7.7 GeV is on the right side of the figure, and

200 GeV is on the left side.
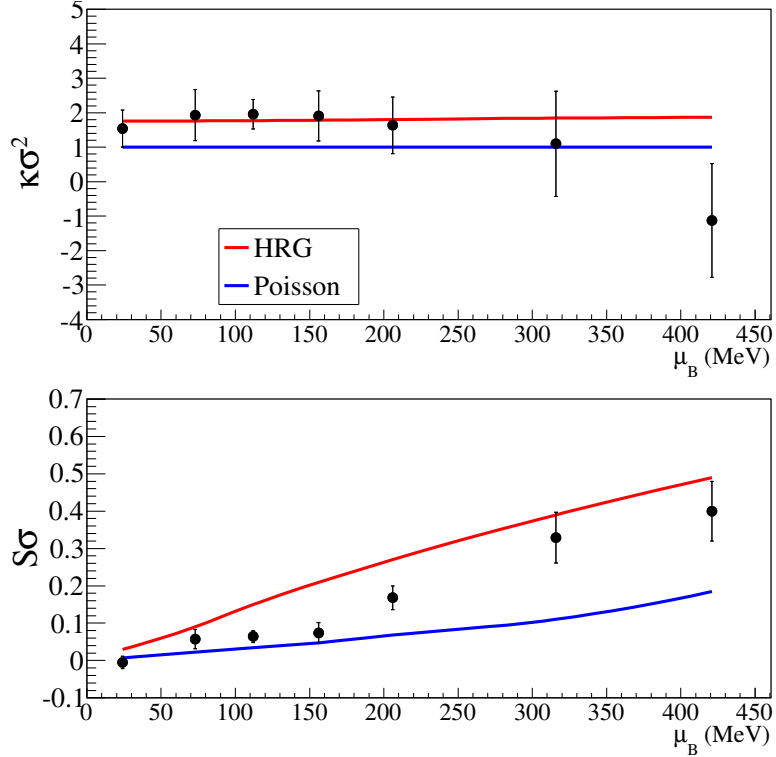
Figure 3.20 : The moments products $S\sigma$ and $K\sigma^2$ for net-charge for 0-5% central collisions versus average baryochemical potential at freezeout (parametrization from Ref. [8]). The blue line is the Poisson expectation, and the red line is the HRG expectation.

In the NLSM, a reasonable value of the width of the critical enhancement is in the range of 50-200 MeV [35]. If the phenomenon of critical opalescence occurs in nuclear matter near the critical point and the actual μ_B width of the critical behavior is close to the 50 MeV lower limit, it is possible that the critical point is in one of these unexplored regions. The region between 11.5 and 19.6 GeV will be explored in the presently underway RHIC run with the collection of a data set at 15 GeV.

RHIC will also collect additional data at $\sqrt{s_{NN}}$ below 20 GeV with high statistics and improved detectors in the so-called "BES Phase-II" run in an upcoming year.

One of the possible detector upgrades may involve expanding the electronics used for the inner sectors of the TPC. These new electronics would increase the number of space points possible from the inner sectors. This would improve the TPC dE/dx PID and also extend the psuedorapidity reach of the TPC. According to Sec. 1.3, this would increase the acceptance of STAR, increasing the binomial parameter p and thereby improving the sensitivity to critical behavior.

Chapter 4

Summary

In collisions at the RHIC, hot and dense systems of strongly interacting nuclear matter called the QGP are created. Multiplicity distributions are an important tool for developing an understanding of the matter created in these collisions. The multiplicity distribution of charged particles can be used to infer the centrality of a collision. The average values of multiplicity distributions of identified particles place the events, on average, in the phase diagram of nuclear matter. In addition, because of their relationship to the susceptibilities of conserved quantities and the correlation length of the system, the moments products of the multiplicity distributions can be used in the search for QGP-to-hadron-gas transitional behavior and for a possible critical point.

By varying the beam energy, the RHIC can, on average, explore different regions of the phase diagram. A combination of the TPC and TOF detectors at STAR allows one to directly identify charged particles in events up to high momenta. Since the moments products are very sensitive to sources of experimental fluctuations, great care must be taken to obtain clean data. Centrality autocorrelations, which artificially lower the values of the moments products, were suppressed by the choice of the multiplicity used to define the centrality. Five different baselines were used in order to look for the possible beam-energy-localized enhancements of the moments products that would be indicative of critical behavior.

The centrality and beam-energy dependence of the third ($S\sigma$) and fourth ($K\sigma^2$)

moments products of various charged particles were investigated versus the centrality in eight different centrality bins. In general, the moments products values were larger than those from the Poisson expectation for net-charge and net-Kaons. For the 0-5% central collisions, the Poisson, the Hadron Resonance Gas, and the mixed-events approaches failed to describe the net-charge moments products values. The failure of the mixed-events description of the net-charge data indicates that intra-event correlations are important. The (N)BD baseline described the net-charge $S\sigma$ values well. The mixed-event values and (N)BD baselines describe the net-proton and net-kaon moments products very well at all centralities and beam energies. In 0-5% central collisions, the total- and net-proton moments products were below the Poisson expectation but were very well described by the mixed-event values.

In the presently available data, no large beam-energy or centrality-localized enhancement of the moments products is observed. The moments products are generally in good, if not excellent, agreement with the (negative) binomial distributions and the mixed-event approach. The $\bar{p}/p$-gating method allows one to constrain the events on the phase diagram more tightly than possible via tight centrality selection alone, yet this approach also does not indicate a strong signal for the CP. It is possible that additional data at beam energies below 20 GeV with improved detectors might allow for more sensitive searches for the CP. However, there does not appear to be any evidence for the existence of the CP in the present data.

Bibliography

[1] J. Adams *et al.*, *Phys. Rev. Lett.*, vol. 91, p. 072304, 2003.

[2] S. Shu for the STAR Collaboration *Nucl. Phys. A*, vol. 830, p. 187, 2009.

[3] http://www.youtube.com/watch?v=xrL2ELkQOie.

[4] M. Miller *et al.*, *Ann. Rev. Nucl. Part. Sci.*, vol. 57, p. 205, 2007.

[5] S. Wheaton *et al.*, *Comp. Phys. Comm.*, vol. 180, p. 84, 2009.

[6] P. Braun-Munzinger *et al.*, *Phys. Letter. B*, vol. 465, p. 15, 1999.

[7] P. Braun-Munzinger *et al.*, "Particle production in heavy ion collisions," Quark Gluon Plasma 3, World Scientific Publishing, 2003.

[8] J. Cleymans *et al.*, *Phys. Rev. C*, vol. 73, p. 034905, 2006.

[9] S. Das for the STAR Collaboration, "Search for the QCD Critical Point by Higher Moments of Net-proton Multiplicity Distributions at STAR," Quark Matter 2012 proceedings, 2012.

[10] M. Stephanov, *Phys. Rev. Lett*, vol. 102, p. 032301, 2009.

[11] S. Ejiri, "Recent progress in lattice QCD at finite density," POS, XXVI Int'l Symp. on Lattice Field Theory, 2008.

[12] M. M. Aggarwal *et al.*, *arXiv:1007.2613*, 2010.

[13] M. Cheng *et al.*, *Phys. Rev. D*, vol. 79, p. 074505, 2009.

[14] M. Stephanov, "QCD phase diagram: an overview," POS, XXIV Int'l Symp. on Lattice Field Theory, 2006.

[15] M. Asakawa and K. Yazaki, *Nucl. Phys. A*, vol. 504, p. 668, 1989.

[16] A. Barducci *et al.*, *Phys. Lett. B*, vol. 231, p. 463, 1989.

[17] A. Barducci *et al.*, *Phys. Rev. D*, vol. 49, p. 426, 1994.

[18] J. Berges and K. Rajagopal, *Nucl. Phys. B*, vol. 538, p. 668, 1989.

[19] M. Halasz *et al.*, *Phys. Rev. D*, vol. 58, p. 096007, 1998.

[20] O. Scavenius *et al.*, *Phys. Rev. C*, vol. 64, p. 045202, 2001.

[21] N. Antoniou and A. Kapoyannis, *Phys. Lett. B*, vol. 563, p. 165, 2003.

[22] Y. Hatta and T. Ikeda, *Phys. Rev. D*, vol. 67, p. 014028, 2003.

[23] A. Barducci *et al.*, *Phys. Rev. D*, vol. 72, p. 056002, 2005.

[24] S. Roessner *et al.*, *arXiv:hep-ph/0609281*.

[25] Z. Fodor and S. Katz, *JHEP*, vol. 0203, p. 014, 2002.

[26] S. Ejiri *et al.*, *Prog. Theor. Phys. Suppl*, vol. 153, p. 118, 2004.

[27] R. Gavai and S. Gupta, *Phys. Rev. D*, vol. 71, p. 114014, 2005.

[28] O. Philipsen, "Status of the QCD phase diagram from lattice calculations," Three Days on Quarkyonic Island, HIC for FAIR workshop, 2011.

[29] G. Endrodi *et al.*, *J. High Energy Phys.*, vol. 1104, p. 1, 2011.

[30] S. Borsanyi, *arXiv:1210.6901v1.*

[31] T. Andrews, *Phil. Trans. Royal Soc.*, vol. 159, p. 575, 1869.

[32] A. Einstein, *Annalen der Physik*, vol. 33, p. 1275, 1910.

[33] L. Landau and E. Lifshitz, *Statistical Physics, Volume 5.* Butterworth-Heinemann, 1980.

[34] B. Berdnikov and K. Rajagopal, *Phys. Rev. D*, vol. 61, p. 105017, 2000.

[35] C. Athanasiou *et al.*, *Phys. Rev. D*, vol. 82, p. 074008, 2010.

[36] M. Stephanov, *Phys. Rev. Lett.*, vol. 107, p. 052301, 2011.

[37] R. Gavai and S. Gupta, *Phys. Rev. D*, vol. 78, p. 114503, 2008.

[38] A. Bzdak and V. Koch, *arXiv:1206.4286v2*, 2012.

[39] A. Franz *et al.*, *Nucl. Instrum. Methods A*, vol. 566, p. 54, 2006.

[40] A. Schmah, private communication, 2013.

[41] M. Anderson *et al.*, *Nucl. Instr. and Meth. A*, vol. 499, p. 659, 2003.

[42] W.J. Llope, *Nucl. Instrum. Methods*, vol. 661, pp. S110 – S113, 2012.

[43] W.J. Llope, *Nucl. Instrum. Methods A*, vol. 522, p. 252, 2004.

[44] B. Bonner *et al.*, "A single Time-of-Flight tray based on multigap resistive plate chambers for the STAR experiment at RHIC," Proceedings of the Sixth International Workshop on Resistive Plate Chambers and Related Detectors, 2003.

[45] D. McDonald, "Calibration of the STAR Time-of-Flight Detector for Particle Identification," Master's thesis, Rice University, 2010.

[46] M. M. Aggarwal *et al.*, *Phys. Rev. Lett*, vol. 105, p. 022302, 2010.

[47] X. Luo for the STAR Collaboration, "Centrality dependence of freeze-out parameters from the beam energy scan at STAR," Quark Matter 2012 proceedings, 2012.

[48] X. Luo, *J. Phys. Conf. Ser*, vol. 316, p. 012003, 2011.

[49] E. Sangaline and L. Chen, private communication, 2011.

[50] B. Efron, *SIAM Review*, vol. 21, p. 460, 1979.

[51] X. Luo, *J. Phys. G*, vol. 39, p. 025008, 2012.

[52] F. Karsch and K. Redlich, *Phys. Lett. B*, vol. 695, p. 136, 2011.

[53] A. Andronic *et al.*, *Nucl. Phys. A*, vol. 772, p. 167, 2006.

[54] G. Torrieri *et al.*, *J. Phys. G*, vol. 37, p. 094016, 2010.

[55] T. Tarnowsky and G. Westfall, *arXiv:nucl-ex/1210.8102v1*, 2012.

[56] W.J. Llope, private communication, 2012.